

1 **Spectral Intensity Bioaerosol Sensor (SIBS):**
2 **An Instrument for Spectrally Resolved Fluorescence Detection**
3 **of Single Particles in Real-Time**

4
5 Tobias Könemann¹, Nicole Savage^{2a}, Thomas Klimach¹, David Walter¹, Janine Fröhlich-
6 Nowoisky¹, Hang Su¹, Ulrich Pöschl¹, J. Alex Huffman², and Christopher Pöhlker¹

7
8 ¹*Max Planck Institute for Chemistry, Multiphase Chemistry Department, P.O. Box 3060, D-55020*
9 *Mainz, Germany*

10 ²*University of Denver, Department of Chemistry and Biochemistry, 2190 E. Iliff Ave., Denver, Col-*
11 *orado 80208, USA*

12
13 ^a *Now at Aerosol Devices Inc., 430 North College Avenue # 430, Fort Collins, Colorado 80524,*
14 *USA*

15
16
17
18 *Correspondence to: J. A. Huffman (alex.huffman@du.edu) and C. Pöhlker (c.pohlker@mpic.de)*

19
20
21
22
23
24
25
26
27 Keywords: WIBS, bioaerosols, fluorescence spectroscopy, performance evaluation and characteriza-
28 tion, polystyrene latex spheres, biofluorophores, size and fluorescence calibration

29 **Abstract**

30 Primary biological aerosol particles (PBAP) in the atmosphere are highly relevant for the Earth sys-
31 tem, climate, and public health. The analysis of PBAP, however, remains challenging due to their
32 high diversity and large spatiotemporal variability. For real-time PBAP analysis, light-induced fluo-
33 rescence (LIF) instruments have been developed and widely used in laboratory and ambient studies.
34 The interpretation of fluorescence data from these instruments, however, is often limited by a lack of
35 spectroscopic information. This study introduces an instrument – the Spectral Intensity Bioaerosol
36 Sensor (SIBS, Droplet Measurement Technologies (DMT, Longmont, CO, USA)) – that resolves
37 fluorescence spectra for single particles and, thus, promises to expand the scope of fluorescent PBAP
38 quantification and classification.

39
40 The SIBS shares key design components with the latest versions of the Wideband Integrated Bioaer-
41 osol Sensor (WIBS) and the findings presented here are also relevant for the widely deployed WIBS-
42 4A and WIBS-NEO as well as other LIF instruments. The key features of the SIBS and findings of
43 this study can be summarized as follows:

- 44 - Particle sizing yields reproducible linear responses for particles in the range of 300 nm to 20 μm .
45 The lower sizing limit is significantly smaller than for earlier commercial LIF instruments (e.g.,
46 WIBS-4A and the Ultraviolet Aerodynamic Particle Sizer (UV-APS)), expanding the analytical
47 scope into the accumulation mode size range.
- 48 - Fluorescence spectra are recorded for two excitation wavelengths ($\lambda_{\text{ex}} = 285$ and 370 nm) and a
49 wide range of emission wavelengths ($\lambda_{\text{mean}} = 302 - 721$ nm) with a resolution of 16 detection
50 channels, which is higher than for most other commercially available LIF bioaerosol sensors.
- 51 - Fluorescence spectra obtained for 16 reference compounds confirm that the SIBS provides suffi-
52 cient spectral resolution to distinguish major modes of molecular fluorescence. For example, the
53 SIBS resolves the spectral difference between bacteriochlorophyll and chlorophyll *a/b*.
- 54 - A spectral correction of the instrument-specific detector response is essential to use the full fluo-
55 rescence emission range.
- 56 - Asymmetry factor (AF) data were assessed and were found to provide only limited analytical
57 information.
- 58 - In test measurements with ambient air, the SIBS worked reliably and yielded characteristically
59 different spectra for single particles in the coarse mode with an overall fluorescent particle frac-
60 tion of $\sim 4\%$ (3σ threshold), which is consistent with earlier studies in comparable environments.

61 1. Introduction

62 Aerosol particles are omnipresent in the atmosphere, where they are involved in many environmental
63 and biogeochemical processes (e.g., Baron & Willeke, 2001; Després et al., 2012; Fuzzi et al., 2006;
64 Hinds, 1999; Pöschl, 2005; Pöschl & Shiraiwa, 2015). Primary biological aerosol particles (PBAP),
65 also termed bioaerosols, represent a diverse group of airborne particles, consisting of whole or frag-
66 mented organisms including, e.g., bacteria, viruses, archaea, algae, and reproductive units (pollen
67 and fungal spores), as well as decaying biomass (e.g., Deepak & Vali, 1991; Després et al., 2012;
68 Fröhlich-Nowoisky et al., 2016; Jaenicke, 2005; Madelin, 1994; Pöschl, 2005) and can span sizes
69 from few nanometers up to $\sim 100 \mu\text{m}$ (Hinds, 1999; Schmauss and Wigand, 1929). The increasing
70 awareness of the importance of PBAP regarding aerosol-cloud interactions, health aspects, and
71 spread of organisms on local, continental or even intercontinental scales has led to a growing interest
72 by scientific researchers and the public (e.g., Després et al., 2012; Fröhlich-Nowoisky et al., 2016;
73 Yao, 2018).

74 Due to inherent limitations (e.g., poor time resolution and costly laboratory analyses) of tradi-
75 tional off-line techniques (e.g., light microscopy and cultivation-based methods) for PBAP quantifi-
76 cation, several types of real-time techniques have been developed within the last several decades to
77 provide higher time resolution and lower user costs (e.g., Caruana, 2011; Després et al., 2012;
78 Fennelly et al., 2017; Ho, 2002; Huffman and Santarpia, 2017; Jonsson and Tjärnhage, 2014; Sodeau
79 and O'Connor, 2016). One promising category of real-time instruments – meaning that particles are
80 sampled and analyzed both instantly and autonomously – involves application of light- induced flu-
81 orescence (LIF). The main principle of this technique is the detection of intrinsic fluorescence from
82 fluorophores ubiquitous in biological cells, such as those airborne within PBAP. These fluorophores
83 include a long list of biological molecules such as aromatic amino acids (e.g., tryptophan and tyro-
84 sine), co-enzymes (e.g., reduced pyridine nucleotides (NAD(P)H)), flavin compounds (e.g., ribofla-
85 vin), as well as biopolymers (e.g., cellulose and chitin) and chlorophyll (e.g., Hill et al., 2009; Li et
86 al., 1991; Pan et al., 2010; Pöhlker et al., 2012, 2013). Detailed information of biological fluorophores
87 can be found elsewhere (Pöhlker et al., 2012 and references therein).

88 Today, commercial on-line LIF instruments such as the Ultraviolet Aerodynamic Particle Sizer
89 (UV-APS, TSI Inc. Shoreview, MN, USA) and the Wideband Integrated Bioaerosol Sensor (WIBS,
90 developed by the University of Hertfordshire, U.K. and currently licensed and manufactured by
91 Droplet Measurement Technologies (DMT, Longmont, CO, USA)) are commonly applied for re-
92 search purposes. Detailed descriptions of the UV-APS (e.g., Agranovski et al., 2003; Brosseau et al.,
93 2000; Hairston et al., 1997) and the WIBS series (e.g., Foot et al., 2008; Kaye et al., 2000, 2005;
94 Stanley et al., 2011) are given elsewhere. Concisely, the UV-APS uses an $\lambda_{\text{ex}} = 355 \text{ nm}$ laser excita-
95 tion source and spans an emission range between $\lambda_{\text{em}} = 420\text{-}575 \text{ nm}$. In contrast, the WIBS applies

96 two pulsed xenon flash lamps emitting at $\lambda_{\text{ex}}=280$ and 370 nm, whereas fluorescence emission is
97 detected in three detection channels, $\lambda_{\text{em}}=310-400$ nm (at $\lambda_{\text{ex}}=280$ nm) and $\lambda_{\text{em}}=420-650$ nm (at
98 $\lambda_{\text{ex}}=280$ and 370 nm). Both instruments provide spectrally unresolved fluorescence information. The
99 latest WIBS model is currently the WIBS-NEO, whose design is based on a WIBS-4A but with an
100 extended particle size detection range between ~ 500 nm and $30\ \mu\text{m}$ (nominal). Both UV-APS and
101 WIBS models have been examined in a variety of laboratory validations (e.g., Agranovski et al.,
102 2003, 2004; Brosseau et al., 2000; Healy et al., 2012; Hernandez et al., 2016; Kanaani et al., 2007;
103 O'Connor et al., 2013; Saari et al., 2013, 2014; Savage et al., 2017; Toprak & Schnaiter, 2013) and
104 have been deployed to investigate both indoor and outdoor atmospheric aerosol via longer-term
105 measurements (e.g., Bhangar et al., 2014; Calvo et al., 2018; Crawford et al., 2015b; Fernández-
106 Rodríguez et al., 2018; Foot et al., 2008; Gabey et al., 2010, 2013; Gosselin et al., 2016; Healy et al.,
107 2014; Huffman et al., 2010, 2012, 2013; Ma et al., 2019; Perring et al., 2015; Schumacher et al.,
108 2013; Twohy et al., 2016; Ziemba et al., 2016).

109 Although LIF instruments do not offer the same qualitative ability to identify sampled particles
110 as, e.g., off-line microscopy, mass spectrometry, or culture-based methods, they provide size-re-
111 solved information as well as fast sampling and fine-scale temporal information for single particles
112 not accessible with off-line techniques. Nevertheless, these instruments present significant chal-
113 lenges. For example, quantification of PBAP by LIF instruments is hindered by the fact that some
114 biological materials reveal weak fluorescence characteristics that does not rise above detection
115 thresholds (Huffman et al., 2012). In addition to this complication, the detection threshold is not a
116 universally defined parameter and varies for each channel between different units of the same type
117 of instruments (e.g., Hernandez et al., 2016; Savage et al., 2017). Furthermore, unambiguous spec-
118 troscopic characterization of bioparticles is fundamentally challenging, because fluorescence spectra
119 of even individual molecules in condensed matter are relatively broad due to radiative decay path-
120 ways of excited electrons. Further, bioparticles are chemically complex, each comprised of a mixture
121 of at least dozens of types of fluorophores that can each emit a unique emission spectrum that smears
122 together into an even broader fluorescence spectrum from each particle (Hill et al., 2009, 2015; Pan,
123 2015). Another difficulty is that many non-biological particles, such as certain mineral dusts and
124 polycyclic aromatic hydrocarbons (PAHs), may fluoresce, making it more difficult to distinguish
125 patterns arising from biological particles (e.g., Pöhlker et al., 2012 and references therein; Savage et
126 al., 2017). Lastly, most currently available commercial LIF instrumentation are limited to recording
127 data in 1-3 spectrally integrated emission channels, which limits the interpretation of fluorescence
128 information. Recent efforts to apply more complex clustering algorithms to the spectrally unresolved
129 WIBS-type data are proving helpful at adding additional discrimination (e.g., Crawford et al., 2015a;
130 Robinson et al., 2013; Ruske et al., 2017; Savage & Huffman, 2018). For example, it was shown for

131 a rural forest study in Colorado that a cluster derived using WIBS-3 data, assigned to fungal spores
132 (Crawford et al., 2015a), correlated well with the mass concentration of molecular fungal tracers
133 (e.g., arabitol and mannitol) measured with offline chemical techniques (Gosselin et al., 2016). In
134 contrast, the clusters in the same study that were assigned to bacteria correlated only poorly with
135 endotoxins, used as bacterial molecular tracers (Gosselin et al., 2016). This provides evidence of a
136 limitation to using LIF instrumentation with low spectral resolution to separate or identify some
137 PBAP types. Additionally, the bacterial cluster allocation might have also been hampered in that case
138 by the minimum detectable particle size of the WIBS ($\sim 0.8 \mu\text{m}$), resulting in a lower detection effi-
139 ciency for bacteria.

140 The evolution of LIF techniques over the last several decades has significantly expanded our
141 knowledge on spatiotemporal patterns of PBAP abundance in the atmosphere. Nevertheless to further
142 improve the applicability of LIF instrumentation to widespread PBAP detection, it is necessary both
143 to design LIF instrumentation with adequate instrumental properties (e.g., high spectral resolution)
144 and to standardize their operation by characterizing instruments thoroughly with known standards
145 (Robinson et al., 2017). Working toward this goal, a number of LIF instruments have been developed
146 to analyze single bioparticles by collecting resolved fluorescence spectra (e.g., Hill et al., 1999; Pan
147 et al., 2010, 2003; Pinnick et al., 2004; Ruske et al., 2017), however relatively little has been done to
148 offer these commercially. Examples for commercially available instruments providing resolved fluo-
149 rescence spectra are the PA-300 ($\lambda_{\text{ex}} = 337 \text{ nm}$; $\lambda_{\text{em}} = 390 - 600 \text{ nm}$, 32 fluorescence detection chan-
150 nels) (Crouzy et al., 2016; Kiselev et al., 2011, 2013) and the follow-up model Rapid-E ($\lambda_{\text{ex}} = 337$
151 nm ; $\lambda_{\text{em}} = 350 - 800 \text{ nm}$, 32 fluorescence detection channels) (<http://www.plair.ch/>), both manufac-
152 tured by Plair SA, Geneva, Switzerland. In addition to collecting resolved fluorescence spectra, both
153 instruments also provide measurements of the decay of fluorescence signals, also referred to as fluo-
154 rescence lifetime.

155 Introduced here is an instrument for the detection and characterization of individual particles; the
156 Spectral Intensity Bioaerosol Sensor (SIBS, Droplet Measurement Technologies). Technical proper-
157 ties of the instrument are described in detail and its performance is validated with sizing and fluo-
158 rescence particle standards, as well as with particles in ambient air. Due to the dual excitation and spec-
159 trally resolved fluorescence in combination with a broad size detection range, the SIBS has the po-
160 tential to increase the selectivity of fluorescent biological and non-biological particle detection and
161 discrimination. Because the SIBS uses a comparable optical system as the WIBS-4A and WIBS-
162 NEO, technical details presented here are broadly important to a growing community of scientists
163 investigating both indoor and outdoor aerosol. Insights and data presented will thus contribute to
164 ongoing discussions within the community of LIF users and will also stimulate discussions about
165 needs for future instrument improvements.

166 2. Materials and methods

167 2.1 Chemicals and materials

168 Supplemental table S1 summarizes 19 polystyrene latex spheres (PSLs, 5 doped with fluorescent
169 dye) and 6 polystyrene divinylbenzene (PS-DVB) particles, which were purchased from Thermo
170 Fisher (Waltham, MA, USA), Bangs Laboratories Inc. (Fishers, IN, USA), Duke Scientific Corp.
171 (Palo Alto, CA, USA), and Polysciences Inc. (Warrington, PA, USA). A detailed study regarding
172 steady-state fluorescence properties of PSLs and PS-DVB particles used within this study can be
173 found in Könemann et al. (2018). Additionally, we analyzed particles comprised separately of seven
174 pure biofluorophores (tyrosine, tryptophan, NAD, riboflavin, chlorophyll *a* and *b*, and bacteriochloro-
175 rophyll) (Table S2) as well as one microorganism (*Saccharomyces cerevisiae*; baker's yeast, bought
176 at a local supermarket). Table S2 also includes reference particles used for asymmetry measurements,
177 namely iron oxide (Fe₃O₄), carbon nanotubes, and ammonium sulfate. Ultrapure water (MilliQ, 18
178 MΩ) and ≥ 99.8 % ethanol (CAS Nr. 64-17-5, Carl Roth GmbH und Co. KG, Karlsruhe, Germany)
179 were used as solvents.

180

181 2.2 Aerosolization of reference particles

182 PSLs were aerosolized from aqueous suspensions with a portable aerosol generator (AG-100; DMT).
183 For both fluorescent and non-fluorescent PSLs, one drop of the suspension (or alternatively three
184 drops for 3 and 4 μm PSLs) was diluted into 10 ml ultrapure water in plastic medical nebulizers
185 (Allied Healthcare, St. Louis, MO, USA). The majority of water vapor from the aerosolization pro-
186 cess condenses inside the mixing chamber (~570 cm³) of the aerosol generator. By using a tempera-
187 ture and relative humidity (RH) sensor (MSR 145 data logger, MSR Electronics GmbH, Seuzach,
188 Switzerland) monitoring the flow directly after the aerosol generator we measured RH values of
189 ~33% (sample flow: 1.4 l/min, dilution: 5 l/min), ~39% (sample flow: 1.4 l/min, dilution: 4 l/min),
190 and ~54% (sample flow: 2.3 l/min, dilution: 2 l/min). Because of the low RH measured, we did not
191 use additional drying (e.g., diffusion dryer) to decrease humidity in the sample flow. Hence, the outlet
192 of the aerosol generator was directly connected to the SIBS inlet with ~30 cm of conductive tubing
193 (1/4 inch). PSLs were measured for 1 min. Non-fluorescent 4.52 μm PSLs were measured for 2 min,
194 because of the low number concentrations due to poor aerosolization efficiency and gravitational
195 settling of larger particle sizes.

196 *S. cerevisiae* was analyzed using a method similar to the one stated above, with the exceptions
197 that the suspension was prepared with a spatula tip of material mixed into ultrapure water and that a
198 diffusion dryer (20 cm, 200 g silica) was added to remove excess water vapor. *S. cerevisiae* was

199 measured for 5 min. Chlorophyll *a*, *b*, and bacteriochlorophyll samples were diluted in 10 ml ethanol.
200 Between each measurement, the setup was cleaned by aerosolizing ultrapure water for 5 min.

201 PS-DVB particles and biofluorophores (Table S1 and S2) were aerosolized in a dry state. For this
202 purpose, air at a flowrate of ~ 0.6 l/min was sent through a HEPA filter into a 10 ml glass vial. A
203 small amount of each solid powder sample (~ 1 g) was placed inside the vial and entrained into the
204 particle-free airstream. Additionally, the sample was physically agitated by tapping the vial. The
205 outlet was connected with ~ 20 cm conductive tubing into the inlet of the SIBS. The tubing and glass
206 vial were cleaned after each measurement to prevent particle contaminations from previous measure-
207 ments. Each powder was sampled until cumulative number concentrations > 5000 particles were
208 reached.

209 In contrast to the monodisperse and spherical PSL standards, the biofluorophore aerosolization
210 process provided a polydisperse and morphologically heterogeneous particle distribution with sig-
211 nificant particle fractions at sizes < 1 μm . Therefore, we only used particles in a size range between
212 1 and 2 μm with sufficient fluorescence intensity values for subsequent data analysis. The only ex-
213 ceptions are the chlorophyll types, where a size range between 0.5 and 2 μm (chlorophyll *a* and *b*)
214 and 0.5 and 1 μm (bacteriochlorophyll) were used due to a less efficient particle aerosolization.

215 The fluorescent background of the SIBS was measured daily by firing the xenon lamps into the
216 optical chamber in the absence of particles (forced trigger mode). In this case, the diaphragm pump
217 was turned off and the inlet blocked to prevent particles reaching the optical chamber. One forced
218 trigger mode was performed per day with 100 xenon shots per min over a duration of 5 min. The
219 average background signal ($+ 1\sigma$ standard deviation (SD)) was subtracted from derived fluorescence
220 emission of each sample. Additionally, the background signal was reviewed periodically between
221 each biofluorophore measurement to verify that, e.g., optical components were not coated with resi-
222 dues from previous measurements. No significant changes in background signal were observed be-
223 tween individual measurements. Optimization of the thresholding strategy is still an on-going work,
224 for example to investigate whether the often applied 3σ threshold used for the WIBS (e.g., Gabey et
225 al., 2010) also works well with respect to the optical setup of the SIBS. For the assessment of the
226 accuracy of measured fluorescence emissions from reference compounds, a threshold of 1σ was used
227 here.

228 For particle asymmetry measurements, iron (II, III) oxide (Fe_3O_4), carbon nanotubes, and ammo-
229 nium sulfate were aerosolized in dry state, and 2 μm non-fluorescent PSLs and ultrapure water were
230 aerosolized with the aerosol generator method outlined above with SIBS integration times of 3 min
231 in all cases. Due to the broad distribution of asymmetry factor (AF) values for particles below 1 μm ,
232 only the size fraction ≥ 1 μm was used for subsequent analyses. Furthermore, we observed that AF
233 bins between 0 and 1, and AF bin 100 tend to produce increased signal responses, especially for high

234 particle concentrations, for which they were discarded within the analyses. The origin of this effect
235 is unknown. However, one explanation could be optical coincidences caused by high particle con-
236 centrations, resulting in multiple particles being simultaneously present within the scattering volume,
237 as reported by Cooper (1988) using forward-scattering signatures of cloud probes.

238 For collection of particles for microscopy measurements, the sample flow was bypassed and led
239 through a custom-made particle impactor, which was connected to a mass flow controller (D-6321-
240 DR, Bronkhorst High-Tech B.V., Ruurlo, Netherlands) and a membrane pump (N816.1.2KN.18,
241 KNF, Freiburg, Germany). Particles were collected out of the sample flow onto glass cover slips (15
242 mm diameter) at a flow rate of 2 l/min over a duration of 1 min.

243

244 **2.3 Reference fluorescence spectra**

245 A Dual-FL fluorescence spectrometer (Horiba Instruments Incorporated, Kyoto, Japan) was used as
246 an offline reference instrument to validate the SIBS spectra. Aqualog V3.6 (Horiba) software was
247 used for data acquisition. The spectrometer was manufacturer-calibrated with NIST Fluorescence
248 Standard Reference Materials (SRMs 2940, 2941, 2942, and 2943). Aforementioned standard fluor-
249 ophores were analyzed using the SIBS excitation wavelengths at $\lambda_{\text{ex}} = 285$ and 370 nm. The Dual-
250 FL¹ spectrometer uses a xenon arc lamp as excitation source and a CCD (charge-coupled device) as
251 emission detector, capable of detecting fluorescence emission between 250 and 800 nm. Unless oth-
252 erwise stated, a low detector gain setting (2.25 e⁻ per count) and an emission resolution of 0.58 nm
253 was used for all measurements with the Dual-FL. Subsequently, we use the term “reference spectra”
254 for all measurements performed with the Dual-FL. In total, 100 individual spectra were recorded for
255 each sample and averaged spectra were analyzed in Igor Pro (Wavemetrics, Lake Oswego, Oregon
256 USA). Background measurements (solvent in the absence of particles) were taken under the same
257 conditions as for sample measurements and subtracted from the emission signal. For direct compar-
258 ison to spectra recorded by the SIBS, reference spectra were re-binned by taking the sum of the
259 fluorescence intensity within the spectral bin width of each SIBS detection channel (Table 1).

260 For PSL measurements, 1.5 μl of each PSL stock solution was diluted in 3.5 ml ultrapure water
261 in a 10 x 10 x 40 mm UV quartz cuvette (Hellma Analytics, Müllheim, Germany) and constantly
262 stirred with a magnetic stirrer to avoid particle sedimentation during measurements. Chlorophyll *a*
263 and *b* and bacteriochlorophyll were handled equally, however concentrations were individually ad-
264 justed to prevent the detector from being saturated and to avoid self-quenching or inner filter effects
265 (Sinski and Exner, 2007). Concentrations were used as follows: chlorophyll *a*: 300 nmol/l, chloro-
266 phyll *b*: 1 $\mu\text{mol/l}$, and bacteriochlorophyll: 3 $\mu\text{mol/l}$. PSLs, chlorophyll *b*, and bacteriochlorophyll

¹ Technical information taken from Dual-FL operation manual, rev. A, 30 NOV 2012; Horiba.

267 measurements were performed with an integration time of 2 s. For chlorophyll *a* an integration time
268 of 1 s was used.

269 All other biofluorophores, *S. cerevisiae*, and PS-DVB particles were measured in dry state using
270 a front surface accessory (Horiba). The sample was placed into the surface holder and covered with
271 a synthetic fused silica window. To limit detector saturation from more highly fluorescent particle
272 types, the surface holder was placed at a 70° angle to the fluorescence detector for NAD and ribofla-
273 vin, 75° for tyrosine, 80° for *S. cerevisiae*, and 85° for tryptophan and PS-DVB particles and subse-
274 quently excited at $\lambda_{\text{ex}}=285$ and 370 nm. Emission resolution and detector gain settings were used as
275 for measurements of samples in solution, except for an integration time of 1 s for all dry samples.
276 Background measurements were performed as described above and subtracted from each sample.
277 Excitation-emission matrices (EEMs) were measured with the same samples as for single wavelength
278 measurements. EEMs were recorded at excitation wavelengths between $\lambda_{\text{ex}} = 240$ and 800 nm (1 nm
279 increments) and an emission range between $\lambda_{\text{em}} = 247$ and 829 nm (0.58 nm increments). Exposure
280 times of 1 s were used, except for 2 μm green, 3 μm non-fluorescent PSLs (2 s), and NAD (0.5 s).
281 EEMs were analyzed using Igor Pro.

282

283 **2.4 Calibration lamps and spectral correction**

284 The relative responsivity of a fluorescence detector can vary substantially across its emission range
285 and, therefore, must be spectrally corrected as a function of emission wavelength (e.g., DeRose, 2007;
286 Lakowicz, 2004). For spectral correction it was important to choose: (i) light sources covering the
287 full spectral emission range of the SIBS, with temporal stability on the timescale of many months
288 and (ii) a calibrated and independent spectrometer to serve as spectral reference.

289 A deuterium-halogen lamp (DH-Mini; Ocean Optics, Largo, FL, USA) and a halogen projector
290 lamp (EHJ 24 V, 250 W; Ushio Inc., Tokyo, Japan) were used as calibration light sources. Both
291 lamps were connected to a 50 cm optical fiber (FT030, Thorlabs, Newton, NJ, USA) and vertically
292 fixed inside the optical chamber of the Dual-FL spectrometer. An aluminum mirror was attached to
293 the end fitting of the optical fiber, reflecting light in a 90° angle into the detector opening. The pro-
294 jector halogen lamp was allowed to warm up for 30 s before each measurement. For all power levels
295 (100, 150, 200, and 250 W), an integration time of 3 s was used. The DH-Mini was operational for
296 30 min before each measurement. Settings were used as for the projector halogen lamp, however,
297 due to the low emission a high detector gain setting (9 e⁻ per count) was used with an integration time
298 of 25 s. As described in Sect. 2.3, 100 single measurements were taken and averaged (Fig. S1). For
299 the SIBS, both light sources were measured in the same way as for the reference spectra. Measure-

300 ments were performed with a detector amplification at 610 V (see Sect. 4.2). Background measure-
301 ments were taken as described in Sect. 2.2. Projector halogen lamp spectra (at all power levels) were
302 recorded for 3 min, the DH-Mini, due to its low emission intensity, for a duration of 5 min.

303 For the halogen projector lamp, averaged intensity values in each spectral bin were acquired at
304 each power level (150, 200, and 250 W). Spectra measured at 100 W were discarded due to the low
305 and unstable emission at wavelengths shorter than ~ 500 nm (Fig. S1). Reference spectra and spectra
306 recorded by the SIBS were normalized onto the SIBS detection channel 9 ($\lambda_{\text{mean}} = 528.0$ nm), which
307 is, theoretically, the detection channel with the highest responsivity (see Sect. 4.3). The individual
308 spectral correction factors were calculated by dividing the reference spectra by the spectra derived
309 from the SIBS. The final correction factors are a combination of both light sources where the detec-
310 tion channels 1-5 ($\lambda_{\text{mean}} = 302.2 - 415.6$ nm) include the correction factors for the DH-Mini and the
311 detection channels 6-16 ($\lambda_{\text{mean}} = 443.8 - 721.1$ nm) the correction factors for the halogen projector
312 lamp. At the intersection between channel 5 and 6, both corrections (DH-Mini, halogen) are in good
313 agreement ($\Delta_{\text{correction}} = 0.6$ in channel 6). For all particle measurements described in the following
314 sections, the background signal and raw sample spectra recorded by the SIBS were multiplied by
315 those correction factors.

316

317 **2.5 Microscopy of selected reference particles**

318 Bright field microscopy was conducted using an Eclipse Ti2 (Nikon, Tokyo, Japan) with a 60x im-
319 mersion oil objective lens and an additional optical zoom factor of 1.5, resulting in a 90x magnifica-
320 tion. Glass cover slips, used as collection substrates in the particle impactor (Sect. 2.2), were put onto
321 a specimen holder and fixed with tape. Images were recorded using a DS Qi2 monochrome micro-
322 scope camera with 16.25 megapixels and z-stacks of related images were created using the software
323 NIS-Elements AR (both Nikon).

324

325 **2.6 Ambient measurement setup and data analysis**

326 The SIBS was operated between the 5th of April to the 7th of May 2018 from a fourth floor roof
327 laboratory at the Max Planck Institute for Chemistry in Mainz, Germany (49°59'28.2"N,
328 8°13'44.5"E) similar to measurements as described in Huffman et al. (2010) using a UV-APS. The
329 period between the 12th and 18th of April 2018 is described here to highlight the capability of the
330 SIBS to monitor ambient aerosol. Beside of the SIBS, four additional instruments (data not shown
331 within this study) were connected with ~ 20 cm conductive tubing ($1/4$ inch) to a sample airflow
332 splitter (Grimm Aerosol Technik GmbH & Co. KG, Ainring, Germany). The splitter was connected
333 to 1.5 m conductive tubing ($5/8$ inch), bent out of the window, and connected to 2.4 m stainless steel

334 tubing ($\frac{5}{8}$ inch, Dockweiler AG, Neustadt-Glewe, Germany) vertically installed. Between a TSP
335 head (total suspended particles, custom-made) and the stainless steel tubing, a diffusion dryer (1 m,
336 1 kg silica) was installed. Silica was exchanged every third to fourth day and periodic forced trigger
337 measurements were performed daily. The total flow was ~ 8.4 l/min.

338 For measurements presented here, particles were only included if they showed fluorescence emis-
339 sion in at least two consecutive spectral channels. This filter was applied to limit noise introduced
340 from measurement artifacts from a variety of sources and will need to be investigated in more detail.
341 The conservative analysis approach here suggests that the values reported are likely to be a lower
342 limit for fluorescent particle number and fraction. The observations are in line with previous meas-
343 urements, however, giving general support that the SIBS measurements are reasonable. Note that the
344 maximum repetition rate of the xenon lamps is 125 Hz, corresponding to maximum concentrations
345 of 20 particles per cm^{-3} (see Sect. 3.3). Because $\sim 50\%$ of the total coarse particle number were excited
346 by xenon 1 and xenon 2, the fluorescent particle concentrations and fluorescent fractions are cor-
347 rected accordingly.

348

349 **3. Design and components of the SIBS**

350 The SIBS is based on the general optical design of the WIBS-4A (e.g., Foot et al., 2008; Healy et al.,
351 2012; Hernandez et al., 2016; Kaye et al., 2005; Perring et al., 2015; Robinson et al., 2017; Savage
352 et al., 2017; Stanley et al., 2011) with improvements based on a lower particle sizing limit, resolved
353 fluorescence detection, and a broader emission range. The instrument provides information about
354 size, particle asymmetry, and fluorescence properties for individual particles in real-time. The exci-
355 tation wavelengths are optimized for the detection of the biological fluorophores tryptophan,
356 NAD(P)H, and riboflavin. However, other fluorophores in PBAP will certainly fluoresce at these
357 excitation wavelengths as many of them cluster in two spectral fluorescence “hotspots” as summa-
358 rized in Pöhlker et al. (2012 and references therein) and as shown for WIBS-4A measurements by
359 Savage et al. (2017). Figure 1 shows an overview of excitation wavelengths and emission ranges of
360 the UV-APS, WIBS-4A, WIBS-NEO, and SIBS for bioaerosol detection in relation to the spectral
361 location of selected biofluorophores, such as tyrosine, tryptophan, NAD(P)H, riboflavin, and chloro-
362 phyll *b*. At $\lambda_{\text{ex}} = 285$ nm, the SIBS excites fluorophores in the “protein hotspot”, at $\lambda_{\text{ex}} = 370$ nm
363 fluorophores in the “flavin/coenzyme hotspot” (Pöhlker et al., 2012). In contrast to the UV-APS, the
364 SIBS is able to detect fluorescence signals from chlorophyll due to the extended upper spectral range
365 of detection (up to $\lambda_{\text{em}} = 721$ nm). Both the WIBS-4A and WIBS-NEO cover the spectral emission
366 range for chlorophyll *b*, however, cannot provide resolved spectral information to separate it from
367 other fluorophores. Table 2 summarizes and compares parameters and technical components of the

368 SIBS, WIBS-4A, and WIBS-NEO. The individual components are described in detail in the subse-
369 quent sections.

370 To avoid potential misunderstanding, it is important to note that the SIBS described in this study
371 is not related to spark-induced breakdown spectroscopy instrumentation, which uses the same acro-
372 nym (e.g., Bauer & Sonnenfroh, 2009; Hunter et al., 2000; Khalaji et al., 2012; Schmidt & Bauer,
373 2010). The DMT SIBS discussed here was recently used as part of a study investigating aerosols in
374 several ambient outdoor environments (Nasir et al., 2018), but the study here is the first to discuss
375 important technical details of the instrument design and operation.

376

377 **3.1 Aerosol inlet and flow diagram**

378 The design for the aerosol inlet of the SIBS is identical to the inlet of the WIBS-4A and WIBS-NEO.
379 A detailed flow diagram is shown in Figure S2. Aerosol is drawn in via an internal pump as laminar
380 air flow through a tapered delivery nozzle (Fig. S2a) where sheath (~2.2 l/min) and sample flow (~0.3
381 l/min) are separated.

382

383 **3.2 Size and shape analysis**

384 After passing the delivery nozzle, entrained particles traverses a 55 mW continuous-wave diode laser
385 at $\lambda = 785$ nm (#2 in Fig. 2 and position #1 in Fig. S3). Unlike in the WIBS-4A and WIBS-NEO (635
386 nm diode laser), the triggering laser in the SIBS is in the near-infrared (IR) region (> 700 nm) and,
387 therefore, outside the detectable emission range of the 16-channel photomultiplier tube (PMT) to
388 avoid scattered light from the particle trigger laser being detected (see Fig. 1). The side and forward
389 scattered light is collected and used for subsequent measurements. Side scattered light is collected
390 by two concave mirrors, which are directed at 90° from the laser beam axis, and reflect the collected
391 light onto a dichroic beam splitter (#7 in Fig. 2). A PMT (H10720-20, Hamamatsu Photonics K.K.,
392 Japan) converts incoming light signals into electrical pulses, which are used for particle triggering
393 and sizing (#6 in Fig. 2). For the determination of the optical particle size, the SIBS uses a calculated
394 calibration curve according to the Lorenz-Mie Theory, assuming spherical and monodisperse PSLs
395 with a refractive index of 1.59 (Brandrup et al., 1989; Lorenz, 1890; Mie, 1908). Compared to aero-
396 dynamic sizing, which depends on particle morphology and density (e.g., Reid et al., 2003; Reponen
397 et al., 2001), the calculated optical diameter can vary significantly if the assumption of sphericity is
398 not fulfilled. In contrast, optical sizing is not as affected by differences in material density. The in-
399 strument operator must thus be aware of uncertainties in measured particle size due to, e.g., particle
400 morphology, spatial orientation of a particle when traversing the trigger laser or changing refractive
401 indices. In contrast to the WIBS-4A, the SIBS and WIBS-NEO detect the full range of particle sizes

402 (SIBS: ~0.3 and 100 μm (nominal); WIBS-NEO: ~0.5 and 30 μm (nominal)) by using one PMT gain
403 setting instead of switching between a “Low Gain” and “High Gain” setting. Physical and technical
404 details of this Gain-switching method are patent pending and are not publicly available.

405 The forward-scattered light is measured by a quadrant PMT (#5 in Fig. 2) to detect the scatter
406 asymmetry for each particle (Kaye et al., 1991, 1996). A OG-515 long pass filter (Schott AG, Mainz,
407 Germany) prevents incoming light from the xenon flash lamps in a spectral range below 515 ± 6 nm
408 from reaching the Quadrant PMT. To calculate the AF, the root-mean-square variations for each
409 quadrant of the PMT of the forward-scattered light intensities are used (Gabey et al., 2010). The AF
410 broadly relates whether a particle is more spherical or fibril. Theoretically, for a perfectly spherical
411 particle, the AF would be 0, whereas an elongated particle would correspond to an AF of 100 (Kaye
412 et al., 1991). However, due to electrical and optical noise of the Quadrant PMT, the AF value of a
413 sphere is usually between ca. 2 and 6 (according to WIBS-4A service manual (DOC-0345 Rev A)).
414 Because the AF value depends on physical properties of optical components, the baseline for spher-
415 ical particles may shift even within identical instruments (Savage et al., 2017). For example, the study
416 by Toprak & Schnaiter (2013) reported an average AF value for spherical particles of 8 using a
417 WIBS-4A. In contrast, AF values shown by Foot et al. (2008) were, on average, below ~5 for
418 spherical particles measured with a WIBS-2s prototype.

419

420 **3.3 Fluorescence excitation**

421 Two xenon flash lamps (L9455-41, Hamamatsu) (#3 and #4 in Fig. 2) are used to induce fluores-
422 cence. They emit light pulses, which exhibit a broad excitation wavelength range of 185 to 2000 nm.
423 The light is optically filtered to obtain a relatively monochromatic excitation wavelength. Further
424 information about spectral properties of the xenon flash lamps can be found elsewhere (Specification
425 sheet TLSZ1006E04, Hamamatsu, May 2015). Figure 3 displays relevant optical properties of the
426 lamps and filters used within the SIBS, WIBS-4A, and WIBS-NEO. For the SIBS, a BrightLine®
427 FF01-285/14-25 (Semrock Inc., Rochester, NY, USA) single-band bandpass filter is used with λ_{mean}
428 = 285 nm and an effective excitation band² of 14 nm width is used for xenon 1. For xenon 2, the
429 single-band bandpass filter BrightLine® FF01-370/36-25 (Semrock) is used with $\lambda_{\text{mean}} = 370$ nm and
430 with an effective excitation band of 36 nm width. The only difference between all three instruments
431 is that the WIBS-4A and WIBS-NEO use a different single-band bandpass filter for xenon 1 (Sem-
432 rock, BrightLine® FF01-280/20-25; $\lambda_{\text{mean}} = 280$ nm; effective excitation band of 20 nm). The exci-
433 tation light beam for all three instruments is focused on the sample flow within the optical cavity,

² The effective excitation band is defined as “guaranteed minimum bandwidth” (GMBW), describing the spectral region a bandpass filter transmits light relative from the mean wavelength. For example, a GMBW of 14 nm means that light is transmitted in a 7 nm spectral range above and below the mean wavelength.

434 resulting in a rectangular beam shape of ~5 mm by 2 mm. Xenon 1 is triggered when particles pass
435 position 2 in Figure S3 and approximately 10 μ s later xenon 2 is triggered as the particles move
436 further to position 3 in Figure S3. After firing, the flash lamps need ~5 ms to recharge. During the
437 recharge period, particles are counted and sized but no fluorescence information is recorded. The
438 maximum repetition rate of the xenon lamps yields a measurable particle number concentration of
439 $\sim 2 \times 10^4 \text{ l}^{-1}$ (corresponding to 20 cm^{-3}).

440 Irradiance values from light sources becomes a crucial factor when interpreting derived fluores-
441 cence data of LIF instruments because the fluorescence intensity is directly proportional to the inten-
442 sity of incident radiant power, described by the relationship:

$$443 \quad F = \phi I_0 (1 - e^{-\epsilon bc}) \quad (1)$$

444 ϕ : quantum efficiency, I_0 : intensity of incident light, ϵ : molar absorptivity, b : path length (cell), c :
445 molar concentration (Guilbault, 1990).

446 To measure the irradiance of each xenon lamp after optical filtering, we used a thermal power
447 head (S425C, Thorlabs), which was placed at a distance of 11.3 cm (focus length from xenon arc
448 bow to sample flow intersection) from the xenon lamp measuring over a duration of 1 min at 10
449 xenon shots per s. By measuring new xenon lamps, we observed an average irradiance of 14.8
450 mW/cm^2 for xenon 1 and 9.6 mW/cm^2 for xenon 2, corresponding to ~154 % higher irradiance (spec-
451 trally integrated) from xenon 1. A second set of lamps, used intermittently for three years including
452 several months of continuous ambient measurements and a lab study with high particle concentra-
453 tions, exhibited average irradiance values of 10.8 mW/cm^2 (1σ SD 1.8 mW/cm^2) for xenon 1 and 4.9
454 mW/cm^2 (1σ SD 1.9 mW/cm^2) for xenon 2, corresponding to ~220 % higher irradiance from xenon
455 1. Comparing the nominal, transmission-corrected irradiance data from the two xenon lamps pro-
456 vided by the lamp supplier (Fig. 3a and 3b, red dashed lines), an irradiance imbalance between xenon
457 1 and xenon 2 can be assumed for all three LIF instruments discussed here (SIBS, WIBS-4A, and
458 WIBS-NEO).

459 Results shown here are comparable to multiple WIBS studies (e.g., Hernandez et al., 2016;
460 Perring et al., 2015; Savage et al., 2017), where fluorescence emission intensities at $\lambda_{\text{ex}} = 280 \text{ nm}$
461 (xenon 1) also show a tendency to be higher than those at $\lambda_{\text{ex}} = 370 \text{ nm}$ (xenon 2).

462 3.4 Spectrally resolved fluorescence detection

463 Fluorescence emission from excited particles is collected by two parabolic mirrors in the optical
464 cavity and delivered onto a custom-made dichroic beam splitter (Semrock, #7 in Fig. 2). The beam

468 splitter allows transmission of incoming light between ~300 and 710 nm, with an average transmis-
469 sion efficiency of 96%. At wavelengths shorter than 300 nm, the transmission decreases rapidly to <
470 20% at 275 nm. At the upper detection end of the SIBS ($\lambda_{\text{mean}} = 721$ nm), the transmission efficiency
471 decreases to ~89%. The scattering light from the diode laser is reflected at a 90° angle onto the PMT
472 used for particle detection and sizing. At the excitation wavelength of 785 nm, the reflection effi-
473 ciency is stated at ~95% (Fig. S4).

474 After passing the dichroic beamsplitter, the photons are led into a grating polychromator (A
475 10766, Hamamatsu) (#8 in Fig. 2). A custom-made transmission grating (Hamamatsu) is used to
476 diffract incoming light within a nominal spectral range between 290.8 – 732.0 nm. In case of the
477 SIBS, a grating with 300 g/mm groove density and 400 nm blaze wavelength is used, resulting in a
478 nominal spectral width of 441.2 nm and a resolution of 28.03 nm/mm. After passing the transmission
479 grating, the diffracted light hits a 16-channel linear array multi-anode PMT (H12310-40, Hamama-
480 tsu) (#9 in Fig. 2) with defined mean wavelengths for each channel as shown in Table 1.

481 For each single particle detected, two spectra are recorded, at $\lambda_{\text{ex}} = 285$ and 370 nm. The detect-
482 able band range of the PMT overlaps the excitation wavelength of xenon 2. Therefore, a notch optical
483 filter (Semrock) is placed between the optical chamber and the grating polychromator to prevent the
484 detector from being saturated. Incoming light at wavelengths shorter than 300 nm and from 362 to
485 377 nm is blocked from reaching the PMT resulting in a reduced spectral bin width for detection
486 channels 1, 3 and 4. The first three detection channels are omitted because their mean wavelengths
487 are below $\lambda_{\text{ex}} = 370$ nm (see also Fig. 1). Accordingly, the emission spectra for xenon 2 excitation
488 begin at channel 4 ($\lambda_{\text{mean}} = 387.3$ nm).

489 Technical data (xenon flash lamps, filters, dichroic beam splitter, PMT responsivity, and trans-
490 mission grating) described in the previous sections (3.3 and 3.4) were provided by Hamamatsu and
491 Semrock. Note that transmission/reflection efficiencies of the dichroic beam splitter, cathode radiant
492 sensitivity of the PMT, and diffraction efficiency data are modeled. Thus, individual components
493 may differ slightly from modeled values, even within the same production batch. Neither company
494 assumes data accuracy or provides warranty, either expressed or implied.

495 The SIBS was originally designed and marketed to record time- and spectrally-resolved fluores-
496 cence lifetimes at two excitation wavelengths. The fluorescence lifetime of most biofluorophores,
497 serving as targets for bioaerosol detection, are usually below 10 ns (e.g., Chorvat & Chorvatova,
498 2009; Herbrich, et al., 2012; O'Connor et al., 2014; Richards-Kortum & Sevick-Muraca, 1996).
499 However, by choosing xenon lamps as excitation source, recording relevant fluorescence lifetimes
500 in this ns range is hampered by the relatively long decay time of the xenon lamp excitation pulse
501 (~1.5 μ s). In principle, fluorescence lifetime measurements would be possible if the xenon lamps
502 were replaced by appropriate laser excitation sources in the SIBS optical design.

503 **3.5 Software components and data output**

504 The SIBS uses an internal computer (#10 in Fig. 2) with embedded LabView-based data acquisition
505 software allowing the user to control functions in real time and change multiple measurement param-
506 eters. As an example, the “Single Particle” tab out of the SIBS interface is shown in Figure S5. Here,
507 the user can define, e.g., the sizing limits of the SIBS (upper and lower threshold) and the minimum
508 size of a particle being excited by the xenon flash lamps. Furthermore, forced trigger measurements
509 can be performed while on this particular tab. Subsequently, the term “forced trigger measurement”
510 will be replaced by “background signal measurement”. A local Wi-Fi network is installed so that the
511 SIBS can be monitored and controlled remotely. A removable hard drive is used for data storage.
512 Data is stored in a HDF5 format to minimize storage space and optimize data write speed. Resulting
513 raw data are processed in Igor Pro. As an example: by using a minimum sizing threshold of 500 nm,
514 the SIBS data output per day, operating in a relatively clean environment (~ 40 particles per cm^{-3}),
515 can span several hundreds of MB. In contrast, the data output can increase up to ~ 3 GB daily in
516 polluted areas (~ 680 particles per cm^{-3}). By lowering the minimum sizing threshold to 300 nm, the
517 data volume can exceed 10 GB per day when sampling in a moderately polluted environment (~ 180
518 particles per cm^{-3}).

519

520 **4. Results and data validation**

521 **4.1 Validation of SIBS sizing**

522 To validate the optical sizing of the SIBS, twenty particle size standards were analyzed, covering a
523 broad size range from 0.3 to 20 μm in particle diameter. Overall, the particle size measurements from
524 the SIBS (optical diameter) show good agreement with the corresponding measurements of physical
525 diameter reported by PSL and PS-DVB manufacturers (Fig. 4). For the SIBS, the manufacturer states
526 a nominal minimum size detection threshold of 300 nm. Figure 4 shows that a linear response be-
527 tween optical particle size and physical particle size extends down to at least 300 nm. Smaller parti-
528 cles were not investigated. The upper size detection threshold is reported by the manufacturer to be
529 nominally 100 μm . However, the upper limit was not investigated here due to the difficulty in aero-
530 solizing particles larger than this. In most field applications, the upper particle size cut is often far
531 below this value due to unavoidable sedimentation losses of large particles in the inlet system (e.g.,
532 Moran-Zuloaga et al., 2018.; Von der Weiden et al., 2009). Note that the size distributions of physical
533 diameter for PS-DVB standards are broader compared to the PSL standards, as reported by the man-
534 ufacturer (Table S1). This also translates to broader distributions of optical diameter measured by the
535 SIBS for PS-DVB than for PSL particles. The 0.356 μm PSL sample was an outlier with respect to
536 the overall trend, showing an optical diameter of 0.54 μm . We suspect that this deviation between

537 physical and optical size can be explained by a poor quality of this particular PSL sample lot rather
538 than an instrumental issue, and so it was not included in the calculation of the trend line (Fig. 4).
539 Furthermore, the SIBS was shown to slightly undersize the PSLs between 0.6 and 0.8 μm , however,
540 the overall trend exhibits a coefficient of determination of $r^2 > 0.998$.

541 As mentioned in Sect. 3.2, an important point regarding the SIBS and WIBS-NEO is that the size
542 calibration within the unit cannot be changed by the user, meaning that the PMT output voltages are
543 transformed directly to outputted physical diameter within the internal computer using a proprietary
544 calculation. It is still important, however, for the user to perform sizing calibration checks frequently
545 to verify and potentially post-correct particle sizing of all particle sizing instruments, including the
546 SIBS and WIBS-NEO.

547

548 **4.2 Amplification of fluorescence detector**

549 As with all optical detection techniques, adequate understanding of detection thresholds is an essen-
550 tial aspect of instrument characterization and use (e.g., Jeys et al., 2007; Savage et al., 2017). Appli-
551 cation of appropriate voltage gain settings must be applied to the physical detection process so as not
552 to lose information about particles that cannot be recovered by post-processing of data. Yet particles
553 in the natural atmosphere exhibit an extremely broad range of fluorescence intensities (many orders
554 of magnitude), arising from the breadth of quantum yields for fluorophores occurring in aerosols and
555 from the steep increase of fluorescence emission intensity with particle size (2^{nd} to 3^{rd} power) (e.g.,
556 Hill et al., 2015; Könemann et al., 2018; Sivaprakasam et al., 2011; Swanson & Huffman, 2018).
557 This range of fluorescence properties is generally broader than the dynamic range of any single in-
558 strument, and so a UV-LIF instrument can be operated, e.g., to either: (i) apply a higher detector gain
559 to allow high sensitivity toward detecting weakly fluorescing particles, often from rather small par-
560 ticles ($< 1 \mu\text{m}$), at the risk of losing fluorescence information for large or strongly fluorescent parti-
561 cles due to detector saturation or (ii) apply a lower detector gain to preferentially detect a wide range
562 of more highly fluorescent particles, but at the risk of not detecting weakly fluorescent or small par-
563 ticles.

564 Amplification voltage of the 16-channel PMT used in the SIBS can be adjusted between 500 and
565 1200 V. Each of the 16 detection channels can also be individually adjusted using digital gain settings
566 within the SIBS acquisition software. This channel-specific gain does not affect the amplification
567 process (e.g., the dynode cascade), but rather modifies the output signal of single detection channels
568 digitally. The digital gain is applied only after the signal collection process, and so cannot compensate
569 for a signal that is below the noise threshold or that saturates the detector. The digital gain was thus
570 left at the maximum gain level (255 arbitrary units (a.u.)) for all channels during particle measure-
571 ments discussed here.

572 To explore the influence of amplification voltage on particle detectability, 0.53 μm purple PSLs
573 were chosen to arbitrarily represent the lower limit of detectable fluorescence intensity. Using larger
574 (0.96 μm) particles comprised of the same purple fluorophore, Könemann et al. (2018) showed that
575 the particles were only narrowly detectable above the fluorescence threshold in each of the three
576 channels of a WIBS-4A (same unit as used in Savage et al., 2017) and so the smaller, 0.53 μm PSLs
577 were chosen here as a first proxy for the most weakly fluorescing particles we would expect to detect.
578 To improve the signal to noise ratio (SNR) for the lower fluorescence detection limit, the PMT ampli-
579 fication voltage was varied in seven steps between 500 and 1000 V (corresponding to a gain from
580 10^3 to 10^6 , specification sheet TPMP01060E02, Hamamatsu, June 2016) for purple PSLs and back-
581 ground signals (Fig. 5a). Whereas PSL spectra at a PMT amplification of 500 V were indistinguish-
582 able from the background signal ($+ 1\sigma$ SD), spectra show a discernable peak at $\lambda_{\text{mean}} = 415.6$ nm
583 above 600 V. Subsequently, the SIBS was operated with a PMT amplification voltage of 610 V
584 corresponding to the lowest SNR threshold accepted (Fig. 5a, b). The detection of small biological
585 particles was tested by measuring the emission spectrum of *S. cerevisiae* as an example of a PBAP
586 (see also Pöhlker et al., 2012). On average, the size of intact *S. cerevisiae* particles range between ~ 2
587 $- 10$ μm (e.g., Pelling et al., 2004; Shaw et al., 1997). To test the ability of the SIBS to detect low
588 intensity emissions, we separately analyzed *S. cerevisiae* particles between 0.5 and 1 μm , which most
589 likely includes cell fragments caused by the aerosolization process (Fig. 5c). The tryptophan-like
590 emission, peaking in detection channel 2 ($\lambda_{\text{mean}} = 330.6$ nm) for $\lambda_{\text{ex}} = 285$ nm, reveals intensity values
591 below 100 a.u., which are comparable to fluorescence intensity values derived from 0.53 μm purple
592 PSLs (detection channel 5, $\lambda_{\text{mean}} = 415.6$ nm, Fig. 5d). These two tests for *S. cerevisiae* and 0.53 μm
593 purple PSLs confirmed the instruments ability to detect emission spectra from particles at least as
594 strongly fluorescent as these two test cases, leaving a wide range to detect larger and more intensely
595 fluorescing particles. By using a 3σ SD threshold, the fluorescence peak at $\lambda_{\text{mean}} = 415.6$ nm of 0.53
596 μm purple PSLs is still detectable but cannot be distinguished from the background signal at a 6σ SD
597 threshold anymore. Therefore, fluorescence intensity values at the lower detection limit should be
598 treated with care. Corrected spectra of both *S. cerevisiae* and 0.53 μm purple PSLs can be found in
599 the supplement (Fig. S6). By operating the SIBS at relatively low detector amplification, very weak
600 fluorescence, especially from small particles (< 1 μm) might not exceed the detection threshold dur-
601 ing field applications and would be missed. Further investigation will be necessary to choose ampli-
602 fication voltages appropriate for individual applications where smaller or otherwise weakly fluores-
603 cent particles might be particularly important. For all subsequent measurements discussed here, a
604 PMT amplification voltage of 610 V was used.

605 Saturation only occurred for 15 and 20 μm non-fluorescent PS-DVB particles. As highlighted in
606 Figure S7, the polystyrene/detergent signal (Könemann et al., 2018) at $\lambda_{\text{ex}} = 285$ nm for 10 μm PS-

607 DVB particles can be spectrally resolved (Fig. S7b), whereas the spectrum for 15 μm PS-DVB par-
608 ticles (Fig. S7e) is altered due to single particles ($\sim 10\%$ out of 400 particles) saturating the detector
609 (at 62383 a.u.). By comparing the defined lower detection end (Fig. 5) to the upper end (Fig. S7), a
610 quantitative difference of approximately three orders of magnitude can be estimated, indicating a
611 wide detectable range at the chosen amplification voltage setting.

612

613 **4.3 Wavelength-dependent spectral correction of detector**

614 The 16 cathodes of the PMT should be considered as independent detectors with wavelength depend-
615 ent, individual responsivity and amplification characteristics. In combination with physical properties
616 of technical components (e.g., excitation sources, optical filters, gratings), an instrumental-specific
617 spectral bias might result in incorrect or misleading spectral patterns if not corrected (e.g., DeRose,
618 2007; DeRose et al., 2007; Holbrook et al., 2006). To compensate for such potential instrumental
619 biases, we used a spectral correction approach as described in Sect. 2.4. The spectral correction fac-
620 tors are comparable to the theoretical responsivity of the PMT with the highest correction for chan-
621 nels 1-4 ($\lambda_{\text{mean}} = 302.2 - 387.3$ nm) and 14-16 ($\lambda_{\text{mean}} = 666.5 - 721.1$ nm) (Fig. 6). Channel 8 ($\lambda_{\text{mean}} =$
622 500.0 nm) shows the highest responsivity and channels 6 and 7 ($\lambda_{\text{mean}} = 443.8$ and 471.9 nm) exhibit
623 a noticeable lower responsivity than their adjacent channels (see also Sect. 4.4.1). The spectral cor-
624 rection shows several peaks (e.g., detector channels 3, 5, and 8) and dips (e.g., detector channels 4,
625 6, and 7) (Fig. 6), however, this pattern is due to gain variations for different channels and is not
626 noise.

627 It is important to note that the detector settings and spectral correction uniquely refer to the SIBS
628 unit as it was used for the current study. Due to technical and physical variability as stated above, it
629 is likely that the spectral correction required for other SIBS units would be somewhat different. Fur-
630 thermore, the wavelength-dependent detector correction may change over time due to material fa-
631 tigue or contaminations in the optical chamber affecting background signal measurements. Periodic
632 surveillance and adjustments are therefore required, especially after measurements where the instru-
633 ment was exposed to high particle concentrations or was operated during extreme weather or envi-
634 ronmental conditions (e.g., temperature, humidity, vibration). For particle sizing verification, we rec-
635 ommend the use of 0.5, 1, and 3 μm non-fluorescent PSLs. Regarding a fluorescence response check,
636 we recommend 2 μm green and 2 μm red PSLs for the validation of the spectral responsivity maxi-
637 mum and the upper (near-IR) detection range. To our knowledge, no fluorescent dyed PSLs are avail-
638 able to verify the response within the lower spectral detection range (UV) of the SIBS. However, the
639 polystyrene signal of 3 μm non-fluorescent PSLs (Fig S7g, h, i, see also Könemann et al., 2018)
640 represents a compromise between signal strength at $\lambda_{\text{ex}} = 285$ nm and aerosolization efficiency (com-
641 pared to PSLs with larger sizes) for a spectral responsivity validation.

642 4.4 Fluorescence spectra of standards

643 4.4.1 PSL standards

644 The SIBS spectra for the four different PSL standards, covering an emission range from UV to near-
645 IR, generally agree well with the corresponding reference spectra (Fig. 7). Each of the two excitation
646 wavelengths probe separate fluorescent modes, which appear at approximately the same emission
647 wavelength for a given PSL type (e.g., $\lambda_{em} = \sim 580$ nm for red PSLs, Fig. 7j), as discussed by
648 Könemann et al. (2018). Moreover, even the rather weak polystyrene and detergent fluorescence,
649 systematically associated with PSL suspensions (Könemann et al., 2018), is resolved by the SIBS at
650 $\lambda_{ex} = 285$ nm and $\lambda_{em} = \sim 300$ nm (Fig. 7b, e, h, k). It is further noteworthy that emission intensity at
651 $\lambda_{ex} = 285$ nm is generally higher than derived emission intensity at $\lambda_{ex} = 370$ nm (Fig. 7c, f, i, l),
652 supporting the finding that a particle receives higher irradiance values from xenon 1 than from xenon
653 2 (see also Sect. 3.3).

654 As mentioned in Sect. 4.3, detection channels 6 and 7 require relatively large correction factors.
655 For 2.07 μm purple PSLs (Fig. 7b, c), the SIBS spectra closely match the references spectra after
656 correction. For the 2.1 μm blue PSLs (Fig. 7e, f), however, the corrected spectrum matches the ref-
657 erence spectrum well, except at detection channel 6 ($\lambda_{mean} = 443.8$ nm), where the SIBS spectrum is
658 lower than the reference spectrum by approximately 50%. This effect was also observed for 1 μm
659 blue PSLs (Thermo Fisher, B0100), doped with the same fluorophore (data not shown). The reason
660 for this discrepancy is unknown. Nevertheless, because this effect only occurs noticeably for highly
661 fluorescent blue PSLs and NAD (see also Sect. 4.4.2), one explanation could be that the instrument-
662 dependent dynode cascade (the electronic amplification stages) for this particular detection channel
663 is suppressed, resulting in a lower amplification efficiency. In this case, relatively low signals could
664 be amplified correctly, whereas medium or high intensity emission could only be amplified up to a
665 certain level. The amplification threshold for detection channel 6 is, however, unknown and needs
666 further verification.

667

668 4.4.2 Biofluorophore standards

669 Figure 8 and 9 highlight fluorescence spectra of different biofluorophores measured by the SIBS,
670 which correspond to related reference spectra (compare also Pöhlker et al., 2012), showing that amino
671 acids (fluorescence emission only at $\lambda_{ex} = 285$ nm), co-enzymes and flavin compounds (fluorescence
672 emission at $\lambda_{ex} = 285$ and 370 nm), and chlorophylls (fluorescence emission only at $\lambda_{ex} = 370$ nm)
673 can be spectrally distinguished.

674 The uncorrected spectrum of tryptophan (Fig. S9) highlights the necessity of a spectral correction
675 to compensate for the low detector responsivity within the UV and near-IR bins. If the fluorescence

676 signal of tryptophan remains uncorrected, the spectra is shifted slightly to longer wavelengths (red-
677 shifted) due to the low responsivity of channel 2 in comparison to channel 3, resulting in misleading
678 spectral information. For NAD (Fig. 8h, i), fluorescence intensity values of channel 6 are lowered
679 due the suppressed amplification efficiency in this particular channel as described for blue PSLs
680 (Sect. 4.4.1).

681 All biofluorophores (except chlorophyll types) were aerosolized as dry powders (see Sect. 2.2)
682 to avoid fluorescence solvatochromism effects (e.g., Johnson et al., 1985). Solvatochromism of fluor-
683 ophores in aqueous solution – the only atmospherically relevant case – typically shifts fluorescence
684 emissions to longer wavelengths due to the stabilized excited state caused by polar solvents
685 (Lakowicz, 2004). This spectral red-shift can be seen in Figure S10, where the peak maximum for
686 NAD shows a difference of ~15 nm between a dry and water-solvated state, whereas riboflavin re-
687 veals an even higher shift of ~37 nm. Here, solvatochromism serves as an example for fluorescence
688 spectra that vary substantially as a function of the fluorophore’s microenvironments (e.g., solvent
689 polarity, pH, temperature).

690 Each of the three types of chlorophyll exhibit the weakest emission of all biofluorophores meas-
691 ured within this study, however the SIBS was able to detect the fluorescence signal at $\lambda_{\text{ex}} = 370$ nm
692 for all three (Fig. 9). The spectral difference between chlorophyll *a* and *b* is only minor at $\lambda_{\text{ex}} = 370$
693 nm ($\Delta\lambda = 8.3$ nm) for which the spectral resolution of the SIBS is not capable of distinguishing be-
694 tween types (Fig. 9a, b, c, d and Fig. S11) (e.g., French et al., 1956; Welschmeyer, 1994). Neverthe-
695 less, the SIBS shows the ability to distinguish between chlorophyll *a* and *b*, and bacteriochlorophyll
696 due to the red-shift in the bacteriochlorophyll spectrum ($\Delta\lambda = 28.5$ nm at $\lambda_{\text{ex}} = 370$ nm, between
697 chlorophyll *a* and bacteriochlorophyll). This may provide a further discrimination level regarding
698 algae, plant residues, and cyanobacteria. Bacteriochlorophyll also shows a second and even stronger
699 emission peak at $\lambda_{\text{ex}} = 370$ nm ($\lambda_{\text{em}} = \sim 800$ nm) that could help further distinguish it from chlorophyll
700 *a* and *b*, but the SIBS spectrometer cannot currently detect this far into the IR (e.g., Rijgersberg et
701 al., 1980; Van Grondelle et al., 1983).

702 Overall, fluorescence emissions recorded by the SIBS are in good agreement with measured ref-
703 erence spectra. However, care must be taken as to the interpretation of fluorescence emissions cov-
704 ering broad spectral ranges, which span regimes with large differences between individual correction
705 factors (e.g., channel 15 ($\lambda_{\text{mean}} = 693.9$ nm, Fig.7l) and channel 2 ($\lambda_{\text{mean}} = 330.6$ nm, Fig.8k). For the
706 SIBS, namely the first two UV detection channels and the last two near-IR channels should be treated
707 with care. Further investigation is required for a careful assessment of how the spectral correction
708 can be applied properly with respect to fluorescent and non-fluorescent atmospheric particles.

709
710

711 **4.5 Particle asymmetry measurements**

712 The AF of spherical particles such as PSLs (Fig. 10a, b) and ultrapure water droplets is approximately
713 10 (Table 3), which is slightly higher than reported values for spherical particles by, e.g., Savage et
714 al. (2017) (AF= ~5) or Toprak & Schnaiter (2013) (AF= ~8) using a WIBS. It is noteworthy that the
715 AF of water droplets increases slightly with increasing droplet size and, therefore, contributes to the
716 mean value (Fig. S13). This effect is most likely based on a decreasing surface tension with increas-
717 ing droplet size for which the droplet morphology is changed to a more oval shape within the sample
718 flow. A similar effect regarding a potential droplet deformation using an Airborne Particle Classifier
719 (APC) was observed by Kaye et al., (1991). Even if the morphology of ammonium sulfate (crystal-
720 line, Fig. 10d) and Fe₃O₄ (irregular clusters, Fig. 10f) is diverse, the difference in AF is only minor
721 (~13 and 14, Table 3), indicating that most naturally occurring aerosols (e.g., sea salt, soot, various
722 bacterial and fungal clusters) will occur in a AF regime between ~10 and 20. Only rod-shaped carbon
723 nanotubes (110-170 nm diameter, 5-9 μm length) show increased AFs with a mean value at ~22
724 (Table 3) at which also, e.g., bacteria would occur (Fig. 10h). No particles observed exhibited average
725 AF values >25, as would have been expected for, e.g., carbon nanotubes. Because the range of AF
726 values for homogenous particles is relatively broad and the differences between morphologically
727 diverse particle types is only minor (Table 3), the question can be raised to what extent particles
728 could be distinguished based on the AF under ambient conditions. Similar broad AF ranges were
729 found in Healy et al., (2012), measuring sodium chloride, chalk, and several pollen and fungal spores
730 types. As also discussed by Savage et al. (2017), the AF values reported by SIBS and WIBS units
731 should be treated with extreme care.

732 The validation of asymmetry measurements is challenging due to unavoidable particle and aero-
733 solization effects (e.g., particle agglomeration and spatial orientation within the sample flow) and the
734 lack of standardized procedures for AF calibrations. Measurements performed in this study do, there-
735 fore, only serve as a rough AF assignment. Moreover, even if both the SIBS and WIBS use the same
736 technical components for defining AFs, a direct intercomparison cannot be applied due to technical
737 variability (e.g., PMT related signal-to-noise ratio or the alignment of optical components). Addi-
738 tionally, it is currently unknown in how far the 785 nm diode laser of the SIBS affect asymmetry
739 measurements compared to the WIBS using a 635 nm diode laser.

740

741 **4.6 Initial ambient measurements**

742 Several weeks of initial ambient SIBS measurements were conducted on the roof of the Max Planck
743 Institute for Chemistry in Mainz, Germany. At a nearby building site, Huffman et al. (2010) con-
744 ducted one of the first ambient UV-APS studies in the year 2006. Moreover, Toprak & Schnaiter

745 (2013) conducted a WIBS-4A study at a comparable site in central Germany from 2010 to 2011. The
746 aim of this brief ambient section is to validate that the SIBS-derived key aerosol and fluorescence
747 data are reasonable and relatively consistent with the aforementioned studies. We found a good agree-
748 ment between the coarse mode ($\geq 1 \mu\text{m}$) number concentrations ($N_{T,c}$) of the SIBS ($N_{T,c}$ ranging from
749 0.25 to 1.59 cm^{-3} , with a mean of 0.76 cm^{-3}) and previous data from the UV-APS (mean $N_{T,c}$: 1.05
750 cm^{-3} (Huffman et al., 2010)) and the WIBS-4A (mean $N_{T,c}$: 0.58 cm^{-3} (Toprak and Schnaiter, 2013))
751 (Fig.11a). Furthermore, good agreement was found between coarse mode fluorescent number con-
752 centrations ($N_{F,c}$) of the SIBS (mean $N_{F,c(3\sigma)}$: 0.025 cm^{-3}), the UV-APS (mean $N_{F,c}$: 0.027 cm^{-3}
753 (Huffman et al., 2010)), and the WIBS-4A (mean $N_{F,c(3\sigma)}$: 0.031 cm^{-3} (Toprak and Schnaiter, 2013))
754 (Fig.11a). Similarly, the fraction of fluorescent particles in the coarse mode ($N_{F,c}/N_{T,c}$) compares well
755 between SIBS (mean $N_{F,c(3\sigma)}/N_{T,c}$: 4.2%), the UV-APS (mean $N_{F,c}/N_{T,c}$: 3.9% (Huffman et al.,
756 2010)), and the WIBS-4A (mean $N_{F,c(3\sigma)}/N_{T,c}$: 7.3% (Toprak and Schnaiter, 2013)) (Fig.11b). Ex-
757 pectedly, a 1σ SD threshold gives much higher SIBS fluorescent fractions of 39.2% , whereas a 6σ
758 SD threshold corresponds with much lower fluorescent fractions of 1% (Fig.11b). Note that no pre-
759 fect match between our results and the studies by Huffman et al. (2010), and Toprak & Schnaiter
760 (2013) can be expected, since the measurements took place with different sampling setups and during
761 different seasons. Furthermore, the spectrally resolved SIBS data makes the definition of fluorescent
762 fraction more complex than for UV-APS and WIBS data (see Sect. 2.6). However, the overall good
763 agreement confirms that the SIBS produces reasonable results in an ambient setting. Further, the
764 single particle fluorescence spectra are reasonable with respect to typical biofluorophore emissions
765 (Pöhlker et al., 2012). Exemplary spectra ($\lambda_{\text{ex}} = 285$ and 370 nm) of ambient single particles can be
766 found in the supplement (Fig.S14). An in-depth analysis of extended SIBS ambient datasets is subject
767 of ongoing work.

768

769 **5. Summary and conclusions**

770 Real-time analysis of atmospheric bioaerosols using commercial LIF instruments has largely been
771 restricted to data recorded in only 1-3 spectrally integrated emission channels, limiting the interpre-
772 tation of fluorescence information. Instruments that can record resolved fluorescence spectra over a
773 broad range of emission wavelengths may thus be required to further improve the applicability of
774 LIF instrumentation to ambient PBAP detection. Introduced here is the SIBS (DMT, Longmont, CO,
775 USA), which is an instrument that provides resolved fluorescence spectra ($\lambda_{\text{mean}} = 302 - 721 \text{ nm}$)
776 from each of two excitation wavelengths ($\lambda_{\text{ex}} = 285$ and 370 nm) for single particles. The current
777 study introduces the SIBS by presenting and experimentally validating its key functionalities. This
778 work critically assesses the strengths and limitations of the SIBS with respect to the growing interest

779 in real-time bioaerosol quantification and classification. It should be noted that the study is an inde-
780 pendent evaluation that was not conducted, endorsed, or co-authored by the manufacturer or repre-
781 sentatives. Overall, this work confirms a precise particle sizing between 300 nm and 20 μm and the
782 particle discrimination ability based on spectrally resolved fluorescence information of several stand-
783 ard compounds.

784 The SIBS was operated at a low PMT detector amplification setting (610 V) to retain capacity to
785 detect large or brightly fluorescent particles. It was confirmed, however, that even weak fluorescence
786 signals from 0.53 μm purple PSLs and from small *S. cerevisiae* fragments (0.5 - 1 μm) can be clearly
787 distinguished from the background signal. Saturation events were only observed for the polysty-
788 rene/detergent signal from relatively large 15 and 20 μm PS-DVB particles. Nevertheless, the fluo-
789 rescence intensity detection threshold is highly instrument-dependent due to the complex interaction
790 of single technical components across individual instruments. For example, xenon 1 exhibited ~154
791 % higher irradiance than xenon 2 (both new lamps) due to differences in the properties of xenon
792 emission and the optical filters used. For used xenon lamps (> 4000 hours of use), an even higher
793 difference of ~220 % was observed. Thus, a defined fluorescence detection threshold will most likely
794 change over time due to, e.g., material fatigue. Additionally, alternating irradiance properties might
795 significantly contribute to observed differences in performance of similar instrument types (e.g.,
796 Hernandez et al., 2016), expressly underlining the need for a fluorescence calibrant applicable across
797 LIF-instruments (e.g., Robinson et al., 2017). Nevertheless, to the best of our knowledge, there is
798 currently no standard reference available that fulfills the requirements to serve as a calibrant for
799 multi-channel, multi-excitation LIF-instruments. Observations in this study are valid not only for the
800 SIBS, but also for the WIBS-4A and WIBS-NEO and lead to important implications for interpretation
801 of particle data. In particular, a particle that exhibits measurable fluorescence in WIBS channel FL1,
802 but only weak fluorescence in channel FL3 could be assigned as an “A-type” particle in one instru-
803 ment but an “AC-type” particle in an instrument with slightly stronger xenon 2 irradiance. These
804 differences in classification can be extremely important to interpretation of ambient data (e.g., Perring
805 et al., 2015; Savage et al., 2017).

806 The PMT used in the SIBS shows a wavelength-dependent sensitivity distribution along all 16
807 detection channels. To compensate for this characteristic and to be able to use the broadest possible
808 fluorescence emission range, the measured emission spectra were corrected with respect to reference
809 spectra acquired from deuterium and halogen lamps. A spectral correction over a broad emission
810 range also introduces drawbacks, however, that LIF-instrument users should keep in mind while in-
811 terpreting derived fluorescence information. In particular, the first two (UV) and the last two (near-
812 IR) detection channels should be treated with care, because they require larger correction factors
813 compared to adjacent channels. Ultimately, the correction factor and amplification voltages applied

814 to the detector will be experiment-specific and will need to be investigated with respect to individual
815 experimental aims. To this extent, possible differences between instruments and important calibra-
816 tions complicate the concept of the instrument being commercially available. Individual users may
817 desire to be able to purchase the SIBS as a “plug-and-play” detector, but using without a critical
818 understanding of these complexities would not be appropriate at this time and could lead to inadvert-
819 ent misinterpretation of the data.

820 Fluorescence spectra of fluorescent PSLs, amino acids, co-enzymes, and flavins measured by the
821 SIBS agree well with corresponding spectra recorded with an offline reference spectrometer. Thus,
822 the SIBS was shown to be capable of clearly distinguishing between different particle types based on
823 resolved fluorescence information. Furthermore, the extended fluorescence emission range ($\lambda_{em} = >$
824 700 nm) enables the SIBS also to distinguish chlorophyll *a* and *b* from bacteriochlorophyll, poten-
825 tially opening new possibilities for the detection of, e.g., algae, plant residues, and cyanobacteria.

826 Particle asymmetry measurements revealed that spherical PSLs have an AF of 9.9 (\pm 3.6),
827 whereas other materials (ammonium sulfate, Fe₃O₄, and carbon nanotubes) show AF values of 13.1
828 (\pm 8.1), 14.4 (\pm 7.4), and 21.6 (\pm 12.7), respectively. Because differences of measured AF value
829 between morphologically diverse particle types are small and within the ranges of uncertainty for the
830 measurement of a given set of particles, it is questionable how well particles can be distinguished
831 based on the AF as presently measured by the quadrant PMT. Users of SIBS and WIBS instruments
832 should apply extreme care if using AF data. It is also likely that different instrument units may have
833 very different AF responses with respect to this measurement. At a minimum, each individual unit
834 needs to be rigorously calibrated to known particle types to determine if AF values are sufficiently
835 different (e.g., separated by several standard deviations) to justify scientific conclusions based on the
836 metric.

837 Exemplary ambient data, measured between the 12th and 18th of April 2018 on the roof of the
838 Max Planck Institute for Chemistry in Mainz (Germany), are consistent with LIF measurement data
839 using a UV-APS (Huffman et al., 2010) and a WIBS-4A (Toprak and Schnaiter, 2013). Total coarse
840 particle number concentrations revealed a mean value of 0.76 cm⁻³ (1.05 cm⁻³ (Huffman et al., 2010);
841 0.58 cm⁻³ (Toprak and Schnaiter, 2013)) of which ~4.2% are considered to be fluorescent using a 3 σ
842 SD threshold (3.9% (Huffman et al., 2010); 7.3% (Toprak and Schnaiter, 2013)), including only par-
843 ticles that show fluorescence emission in at least two adjoining detection channels. Using a 1 σ and
844 6 σ SD threshold results in fluorescent fractions of 39.2% and 1% respectively. However, the applica-
845 bility of different threshold strategies for the SIBS is currently under investigation and needs further
846 verifications.

847 The results suggest that the SIBS has the ability to increase the selectivity of detection of fluo-
848 rescent biological and non-biological particles by use of two excitation wavelengths and 16-channel

849 resolved fluorescence information in combination with a broad detectable emission range. The ap-
850 plicability of described methods onto ambient datasets is currently under investigation. Data shown
851 here and the detailed insights of technical components used in the SIBS will be broadly beneficial
852 for users of LIF instruments providing resolved fluorescence information, but also for users of vari-
853 ous generations of WIBS and other LIF instruments widely applied within the bioaerosol community.

854

855 **6. Data availability**

856 The data of the key results presented here can be provided upon request. For specific data requests,
857 please refer to the corresponding authors.

858

859 **Acknowledgements**

860 This work was supported by the Max Planck Society (MPG) and the Max Planck Graduate Center
861 with the Johannes Gutenberg-University Mainz (MPGC). Financial support for Nicole Savage was
862 provided by the Phillipson Graduate Fellowship from the University of Denver. We thank Maria
863 Praß, Mira Pöhlker, Jan-David Förster, Meinrat O. Andreae, Peter Hoor, Viviane Després, Benjamin
864 Swanson, Jorge Saturno, Bruna Holanda, Florian Ditas, Daniel Moran-Zuloaga, Björn Nillius, Jing
865 Ming, Gavin McMeeking, Gary Granger, Alexis Attwood, Greg Kok, Robert MacAllister, John
866 Walker, Matt Mahin, Matt Freer, Uwe Kuhn, Minghui Zhang, Petya Yordanova, Naama Lang-Yona,
867 and members of the Mainz Bioaerosol Laboratory (MBAL) for their support and stimulating discus-
868 sions.

869 **7. References**

- 870 Agranovski, V., Ristovski, Z., Hargreaves, M., Blackall, P. . and Morawska, L.: Real-time measurement of bacterial
871 aerosols with the UVAPS: performance evaluation, *J. Aerosol Sci.*, 34(3), 301–317, doi:10.1016/S0021-
872 8502(02)00181-7, 2003.
- 873 Agranovski, V., Ristovski, Z. D., Ayoko, G. A. and Morawska, L.: Performance Evaluation of the UVAPS in Measuring
874 Biological Aerosols: Fluorescence Spectra from NAD(P)H Coenzymes and Riboflavin, *Aerosol Sci. Technol.*,
875 38(4), 354–364, doi:10.1080/02786820490437505, 2004.
- 876 Baron, P. A. and Willeke, K.: *Aerosol fundamentals*, *Aerosol Meas. Princ. Tech. Appl.*, 2, 2001.
- 877 Bauer, A. J. R. and Sonnenfroh, D. M.: Spark-induced breakdown spectroscopy-based classification of bioaerosols, in
878 *Safety, Security & Rescue Robotics (SSRR)*, 2009 IEEE International Workshop on, pp. 1–4, IEEE., 2009.
- 879 Bhangar, S., Huffman, J. A. and Nazaroff, W. W.: Size-resolved fluorescent biological aerosol particle concentrations
880 and occupant emissions in a university classroom, *Indoor Air*, 24(6), 604–617, 2014.
- 881 Brandrup, J., Immergut, E. H., Grulke, E. A., Abe, A. and Bloch, D. R.: *Polymer handbook*, Wiley New York etc., 1989.
- 882 Brosseau, L. M., Vesley, D., Rice, N., Goodell, K., Nellis, M. and Hairston, P.: Differences in detected fluorescence
883 among several bacterial species measured with a direct-reading particle sizer and fluorescence detector, *Aerosol*
884 *Sci. Technol.*, 32(6), 545–558, 2000.
- 885 Calvo, A. I., Baumgardner, D., Castro, A., Fernández-González, D., Vega-Maray, A. M., Valencia-Barrera, R. M.,
886 Oduber, F., Blanco-Alegre, C. and Fraile, R.: Daily behavior of urban Fluorescing Aerosol Particles in
887 northwest Spain, *Atmos. Environ.*, 184, 262–277, 2018.
- 888 Caruana, D. J.: Detection and analysis of airborne particles of biological origin: present and future, *Analyst*, 136(22),
889 4641–4652, 2011.
- 890 Chorvat, D. and Chorvatova, A.: Multi-wavelength fluorescence lifetime spectroscopy: a new approach to the study of
891 endogenous fluorescence in living cells and tissues, *Laser Phys. Lett.*, 6(3), 175–193,
892 doi:10.1002/lapl.200810132, 2009.
- 893 Cooper, W. A.: Effects of coincidence on measurements with a forward scattering spectrometer probe, *J. Atmos. Ocean.*
894 *Technol.*, 5(6), 823–832, 1988.
- 895 Crawford, I., Ruske, S., Topping, D. O. and Gallagher, M. W.: Evaluation of hierarchical agglomerative cluster analysis
896 methods for discrimination of primary biological aerosol, *Atmos. Meas. Tech.*, 8(11), 4979–4991, 2015a.
- 897 Crawford, I., Lloyd, G., Bower, K. N., Connolly, P. J., Flynn, M. J., Kaye, P. H., Choularton, T. W. and Gallagher, M.
898 W.: Observations of fluorescent aerosol–cloud interactions in the free troposphere at the Sphinx high Alpine
899 research station, Jungfrauoch, *Atmos. Chem. Phys.*, 15(19), 26067–26088, 2015b.
- 900 Crouzy, B., Stella, M., Konzelmann, T., Calpini, B. and Clot, B.: All-optical automatic pollen identification: Towards
901 an operational system, *Atmos. Environ.*, 140, 202–212, doi:http://dx.doi.org/10.1016/j.atmosenv.2016.05.062,
902 2016.
- 903 Deepak, A. and Vali, G.: *The International Global Aerosol Program (IGAP) plan: Overview (Vol. 1)*, A. Deepak Pub.,
904 1991.
- 905 DeRose, P. C.: *Standard guide to fluorescence: Instrument calibration and validation*, US Department of Commerce,
906 Technology Administration, National Institute of Standards and Technology., 2007.
- 907 DeRose, P. C., Early, E. A. and Kramer, G. W.: Qualification of a fluorescence spectrometer for measuring true
908 fluorescence spectra, *Rev. Sci. Instrum.*, 78(3), 33107, 2007.
- 909 Després, V. R., Huffman, J. A., Burrows, S. M., Hoose, C., Safatov, A. S., Buryak, G., Fröhlich-Nowoisky, J., Elbert,

910 W., Andreae, M. O., Pöschl, U. and Jaenicke, R.: Primary biological aerosol particles in the atmosphere: A
911 review, *Tellus, Ser. B Chem. Phys. Meteorol.*, 64, doi:10.3402/tellusb.v64i0.15598, 2012.

912 Fennelly, M. J., Sewell, G., Prentice, M. B., O'Connor, D. J. and Sodeau, J. R.: The Use of Real-Time Fluorescence
913 Instrumentation to Monitor Ambient Primary Biological Aerosol Particles (PBAP), *Atmosphere (Basel)*., 9(1),
914 1, 2017.

915 Fernández-Rodríguez, S., Tormo-Molina, R., Lemonis, N., Clot, B., O'Connor, D. J. and Sodeau, J. R.: Comparison of
916 fungal spores concentrations measured with wideband integrated bioaerosol sensor and Hirst methodology,
917 *Atmos. Environ.*, 175, 1–14, 2018.

918 Foot, V. E., Kaye, P. H., Stanley, W. R., Barrington, S. J., Gallagher, M. and Gabey, A.: Low-cost real-time
919 multiparameter bio-aerosol sensors, *Proc. SPIE*, 7116, 71160I–71160I–12, doi:10.1117/12.800226, 2008.

920 French, C. S., Smith, J. H. C., Virgin, H. I. and Airth, R. L.: Fluorescence-Spectrum Curves of Chlorophylls,
921 Pheophytins, Phycoerythrins, Phycocyanins and Hypericin., *Plant Physiol.*, 31(5), 369, 1956.

922 Fröhlich-Nowoisky, J., Kampf, C. J., Weber, B., Huffman, J. A., Pöhlker, C., Andreae, M. O., Lang-Yona, N., Burrows,
923 S. M., Gunthe, S. S., Elbert, W., Su, H., Hoor, P., Thines, E., Hoffmann, T., Després, V. R. and Pöschl, U.:
924 Bioaerosols in the Earth System: Climate, Health, and Ecosystem Interactions, *Atmos. Res.*, 182, 346–376,
925 <https://doi.org/10.1016/j.atmosres.2016.07.018>, 2016.

926 Fuzzi, S., Andreae, M. O., Huebert, B. J., Kulmala, M., Bond, T. C., Boy, M., Doherty, S. J., Guenther, A., Kanakidou,
927 M., Kawamura, K., Kerminen, V.-M., Lohmann, U., Russell, L. M. and Pöschl, U.: Critical assessment of the
928 current state of scientific knowledge, terminology, and research needs concerning the role of organic aerosols
929 in the atmosphere, climate, and global change, *Atmos. Chem. Phys.*, 6(7), 2017–2038, doi:10.5194/acp-6-2017-
930 2006, 2006.

931 Gabey, A. M., Gallagher, M. W., Whitehead, J., Dorsey, J. R., Kaye, P. H. and Stanley, W. R.: Measurements and
932 comparison of primary biological aerosol above and below a tropical forest canopy using a dual channel
933 fluorescence spectrometer, *Atmos. Chem. Phys.*, 10(10), 4453–4466, doi:10.5194/acp-10-4453-2010, 2010.

934 Gabey, A. M., Vaitilingom, M., Freney, E., Boulon, J., Sellegri, K., Gallagher, M. W., Crawford, I. P., Robinson, N. H.,
935 Stanley, W. R. and Kaye, P. H.: Observations of fluorescent and biological aerosol at a high-altitude site in
936 central France, *Atmos. Chem. Phys.*, 13(15), 7415–7428, doi:10.5194/acp-13-7415-2013, 2013.

937 Gosselin, M. I., Rathnayake, C. M., Crawford, I., Pöhlker, C., Fröhlich-Nowoisky, J., Schmer, B., Després, V. R.,
938 Engling, G., Gallagher, M., Stone, E., Pöschl, U., and Huffman, J. A.: Fluorescent bioaerosol particle, molecular
939 tracer, and fungal spore concentrations during dry and rainy periods in a semi-arid forest, *Atmos. Chem. Phys.*,
940 16(23), 15165–15184, 2016.

941 Van Grondelle, R., Hunter, C. N., Bakker, J. G. C. and Kramer, H. J. M.: Size and structure of antenna complexes of
942 photosynthetic bacteria as studied by singlet-singlet quenching of the bacteriochlorophyll fluorescence yield,
943 *Biochim. Biophys. Acta (BBA)-Bioenergetics*, 723(1), 30–36, 1983.

944 Guilbault, G. G.: *Practical fluorescence (Vol. 3)*, CRC Press., 1990.

945 Hairston, P. P., Ho, J. and Quant, F. R.: Design of an instrument for real-time detection of bioaerosols using simultaneous
946 measurement of particle aerodynamic size and intrinsic fluorescence, *J. Aerosol Sci.*, 28(3), 471–482,
947 doi:10.1016/S0021-8502(96)00448-X, 1997.

948 Healy, D. A., O'Connor, D. J., Burke, A. M. and Sodeau, J. R.: A laboratory assessment of the Waveband Integrated
949 Bioaerosol Sensor (WIBS-4) using individual samples of pollen and fungal spore material, *Atmos. Environ.*,
950 60, 534–543, doi:10.1016/j.atmosenv.2012.06.052, 2012.

951 Healy, D. A., Huffman, J. A., O'Connor, D. J., Pöhlker, C., Pöschl, U. and Sodeau, J. R.: Ambient measurements of

952 biological aerosol particles near Killarney, Ireland: a comparison between real-time fluorescence and
953 microscopy techniques, *Atmos. Chem. Phys.*, 14(15), 8055–8069, doi:10.5194/acp-14-8055-2014, 2014.

954 Herbrich, S., Gehder, M., Krull, R. and Gericke, K.-H.: Label-free spatial analysis of free and enzyme-bound NAD (P)
955 H in the presence of high concentrations of melanin, *J. Fluoresc.*, 22(1), 349–355, 2012.

956 Hernandez, M., Perring, A. E., McCabe, K., Kok, G., Granger, G. and Baumgardner, D.: Chamber catalogues of optical
957 and fluorescent signatures distinguish bioaerosol classes, *Atmos. Meas. Tech.*, 9(7), 3283–3292, 2016.

958 Hill, S. C., Pinnick, R. G., Niles, S., Pan, Y., Holler, S., Chang, R. K., Bottiger, J., Chen, B. T., Orr, C. and Feather, G.:
959 Real-time measurement of fluorescence spectra from single airborne biological particles, *F. Anal. Chem.*
960 *Technol.*, 3(4-5), 221–239, 1999.

961 Hill, S. C., Mayo, M. W. and Chang, R. K.: Fluorescence of Bacteria, Pollens, and Naturally Occurring Airborne
962 Particles: Excitation / Emission Spectra, *Army Res. Lab. Appl. Phys.*, (February), 2009.

963 Hill, S. C., Williamson, C. C., Doughty, D. C., Pan, Y.-L., Santarpia, J. L. and Hill, H. H.: Size-dependent fluorescence
964 of bioaerosols: Mathematical model using fluorescing and absorbing molecules in bacteria, *J. Quant. Spectrosc.*
965 *Radiat. Transf.*, 157, 54–70, doi:10.1016/j.jqsrt.2015.01.011, 2015.

966 Hinds, W. C.: *Aerosol Technology: Properties, Behavior, and Measurement of airborne Particles* (2nd), 1999.

967 Ho, J.: Future of biological aerosol detection, *Anal. Chim. Acta*, 457(1), 125–148, doi:http://dx.doi.org/10.1016/S0003-
968 2670(01)01592-6, 2002.

969 Holbrook, R. D., DeRose, P. C., Leigh, S. D., Rukhin, A. L. and Heckert, N. A.: Excitation–emission matrix fluorescence
970 spectroscopy for natural organic matter characterization: a quantitative evaluation of calibration and spectral
971 correction procedures, *Appl. Spectrosc.*, 60(7), 791–799, 2006.

972 Huffman, J. A. and Santarpia, J.: Online Techniques for Quantification and Characterization of Biological Aerosols,
973 *Microbiol. Aerosols*, 83–114, 2017.

974 Huffman, J. A., Treutlein, B. and Pöschl, U.: Fluorescent biological aerosol particle concentrations and size distributions
975 measured with an Ultraviolet Aerodynamic Particle Sizer (UV-APS) in Central Europe, *Atmos. Chem. Phys.*,
976 10(7), 3215–3233, doi:10.5194/acp-10-3215-2010, 2010.

977 Huffman, J. A., Sinha, B., Garland, R. M., Snee-Pollmann, A., Gunthe, S. S., Artaxo, P., Martin, S. T., Andreae, M. O.
978 and Pöschl, U.: Size distributions and temporal variations of biological aerosol particles in the Amazon
979 rainforest characterized by microscopy and real-time UV-APS fluorescence techniques during AMAZE-08,
980 *Atmos. Chem. Phys.*, 12, 11997–12019, doi:10.5194/acp-12-11997-2012, 2012.

981 Huffman, J. A., Prenni, A. J., Demott, P. J., Pöhlker, C., Mason, R. H., Robinson, N. H., Fröhlich-Nowoisky, J., Tobo,
982 Y., Després, V. R., Garcia, E., Gochis, D. J., Harris, E., Müller-Germann, I., Ruzene, C., Schmer, B., Sinha, B.,
983 Day, D. A., Andreae, M. O., Jimenez, J. L., Gallagher, M., Kreidenweis, S. M., Bertram, A. K. and Pöschl, U.:
984 High concentrations of biological aerosol particles and ice nuclei during and after rain, *Atmos. Chem. Phys.*,
985 13, 6151–6164, doi:10.5194/acp-13-6151-2013, 2013.

986 Hunter, A. J. R., Morency, J. R., Senior, C. L., Davis, S. J. and Fraser, M. E.: Continuous emissions monitoring using
987 spark-induced breakdown spectroscopy, *J. Air Waste Manage. Assoc.*, 50(1), 111–117, 2000.

988 Jaenicke, R.: Abundance of cellular material and proteins in the atmosphere., *Science*, 308, 73,
989 doi:10.1126/science.1106335, 2005.

990 Jeys, T. H., Herzog, W. D., Hybl, J. D., Czerwinski, R. N. and Sanchez, A.: Advanced trigger development, *Lincoln*
991 *Lab. J.*, 17(1), 29–62, 2007.

992 Johnson, I. D., Thomas, E. W. and Cundall, R. B.: Fluorescence solvatochromism of nitrodiphenylhexatrienes, *J. Chem.*
993 *Soc. Faraday Trans. 2 Mol. Chem. Phys.*, 81(9), 1303–1315, 1985.

994 Jonsson, P. and Tjärnhage, T.: Trends in Biological Detection BT - Bioaerosol Detection Technologies, edited by P.
995 Jonsson, G. Olofsson, and T. Tjärnhage, pp. 317–322, Springer New York, New York, NY., 2014.

996 Kanaani, H., Hargreaves, M., Ristovski, Z. and Morawska, L.: Performance assessment of UVAPS: Influence of fungal
997 spore age and air exposure, *J. Aerosol Sci.*, 38(1), 83–96, doi:10.1016/j.jaerosci.2006.10.003, 2007.

998 Kaye, P. H., Stanley, W. R., Hirst, E., Foot, E. V, Baxter, K. L. and Barrington, S. J.: Single particle multichannel bio-
999 aerosol fluorescence sensor, *Opt. Express*, 13(10), 3583–3593, doi:10.1364/OPEX.13.003583, 2005.

1000 Kaye, P. H., Eyles, N. A., Ludlow, I. K. and Clark, J. M.: An instrument for the classification of airborne particles on
1001 the basis of size, shape, and count frequency, *Atmos. Environ. Part A. Gen. Top.*, 25(3–4), 645–654, 1991.

1002 Kaye, P. H., Alexander-Buckley, K., Hirst, E., Saunders, S. and Clark, J. M.: A real-time monitoring system for airborne
1003 particle shape and size analysis, *J. Geophys. Res. Atmos.*, 101(D14), 19215–19221, 1996.

1004 Kaye, P. H., Barton, J. E., Hirst, E. and Clark, J. M.: Simultaneous light scattering and intrinsic fluorescence
1005 measurement for the classification of airborne particles., *Appl. Opt.*, 39(21), 3738–3745,
1006 doi:10.1364/AO.39.003738, 2000.

1007 Khalaji, M., Roshanzadeh, B., Mansoori, A., Taefi, N. and Tavassoli, S. H.: Continuous dust monitoring and analysis
1008 by spark induced breakdown spectroscopy, *Opt. Lasers Eng.*, 50(2), 110–113, 2012.

1009 Kiselev, D., Bonacina, L. and Wolf, J.-P.: Individual bioaerosol particle discrimination by multi-photon excited
1010 fluorescence, *Opt. Express*, 19(24), 24516–24521, 2011.

1011 Kiselev, D., Bonacina, L. and Wolf, J.-P.: A flash-lamp based device for fluorescence detection and identification of
1012 individual pollen grains, *Rev. Sci. Instrum.*, 84(3), 33302, 2013.

1013 Könemann, T., Savage, N. J., Huffman, J. A. and Pöhlker, C.: Characterization of steady-state fluorescence properties
1014 of polystyrene latex spheres using off-and online spectroscopic methods, *Atmos. Meas. Tech.*, 11(7), 3987–
1015 4003, 2018.

1016 Lakowicz, J. R.: *Principles of Fluorescence Spectroscopy*, (1999), 2004.

1017 Li, J. K., Asali, E. C., Humphrey, A. E. and Horvath, J. J.: Monitoring cell concentration and activity by multiple
1018 excitation fluorometry, *Biotechnol. Prog.*, 7(1), 21–27, doi:10.1021/bp00007a004, 1991.

1019 Lorenz, L.: *Lysbevægelsen i og uden for en af plane Lysbølger belyst Kugle*, na., 1890.

1020 Ma, Y., Wang, Z., Yang, D., Diao, Y., Wang, W., Zhang, H., Zhu, W. and Zheng, J.: On-line measurement of fluorescent
1021 aerosols near an industrial zone in the Yangtze River Delta region using a wideband integrated bioaerosol
1022 spectrometer, *Sci. Total Environ.*, 656, 447–457, 2019.

1023 Madelin, T. M.: Fungal aerosols: A review, *J. Aerosol Sci.*, 25, 1405–1412, doi:10.1016/0021-8502(94)90216-X, 1994.

1024 Mie, G.: Considerations on the optics of turbid media, especially metal sols, *Ann. Phys*, 25, 377–442, 1908.

1025 Moran-Zuloaga, D., Ditas, F., Walter, D., Saturno, J., Brito, J., Carbone, S., Chi, X., Hrabě de Angelis, I., Baars, H.,
1026 Godoi, R. H. M., Heese, B., Holanda, B. A., Lavrič, J. V., Martin, S. T., Ming, J., Pöhlker, M. L., Ruckteschler,
1027 N., Su, H., Wang, Y., Wang, Q., Wang, Z., Weber, B., Wolff, S., Artaxo, P., Pöschl, U., Andreae, M. O., and
1028 Pöhlker, C.: Long-term study on coarse mode aerosols in the Amazon rain forest with the frequent intrusion of
1029 Saharan dust plumes, *Atmos. Chem. Phys.*, 18, 10055-10088, <https://doi.org/10.5194/acp-18-10055-2018>,
1030 2018.

1031 Nasir, Z., Rolph, C., Collins, S., Stevenson, D., Gladding, T., Hayes, E., Williams, B., Khera, S., Jackson, S. and Bennett,
1032 A.: A Controlled Study on the Characterisation of Bioaerosols Emissions from Compost, *Atmosphere (Basel)*,
1033 9(10), 379, 2018.

1034 O'Connor, D. J., Healy, D. A. and Sodeau, J. R.: The on-line detection of biological particle emissions from selected
1035 agricultural materials using the WIBS-4 (Waveband Integrated Bioaerosol Sensor) technique, *Atmos. Environ.*,

1036 80, 415–425, 2013.

1037 O'Connor, D. J., Lovera, P., Iacopino, D., O'Riordan, A., Healy, D. A. and Sodeau, J. R.: Using spectral analysis and
1038 fluorescence lifetimes to discriminate between grass and tree pollen for aerobiological applications, *Anal.*
1039 *Methods*, 6(6), 1633–1639, 2014.

1040 Pan, Y.-L.: Detection and characterization of biological and other organic-carbon aerosol particles in atmosphere using
1041 fluorescence, *J. Quant. Spectrosc. Radiat. Transf.*, 150, 12–35, doi:10.1016/j.jqsrt.2014.06.007, 2015.

1042 Pan, Y.-L., Hill, S. C., Pinnick, R. G., Huang, H., Bottiger, J. R. and Chang, R. K.: Fluorescence spectra of atmospheric
1043 aerosol particles measured using one or two excitation wavelengths: Comparison of classification schemes
1044 employing different emission and scattering results, *Opt. Express*, 18(12), 12436–12457,
1045 doi:10.1364/OE.18.012436, 2010.

1046 Pan, Y.-L., Hartings, J., Pinnick, R. G., Hill, S. C., Halverson, J. and Chang, R. K.: Single-particle fluorescence
1047 spectrometer for ambient aerosols, *Aerosol Sci. Technol.*, 37(8), 628–639, 2003.

1048 Pelling, A. E., Sehati, S., Gralla, E. B., Valentine, J. S. and Gimzewski, J. K.: Local nanomechanical motion of the cell
1049 wall of *Saccharomyces cerevisiae*, *Science* (80-.), 305(5687), 1147–1150, 2004.

1050 Perring, A. E., Schwarz, J. P., Baumgardner, D., Hernandez, M. T., Spracklen, D. V., Heald, C. L., Gao, R. S., Kok, G.,
1051 McMeeking, G. R., McQuaid, J. B. and Fahey, D. W.: Airborne observations of regional variation in fluorescent
1052 aerosol across the United States, *J. Geophys. Res. Atmos.*, 120(3), 1153–1170, doi:10.1002/2014JD022495,
1053 2015.

1054 Pinnick, R. G., Hill, S. C., Pan, Y. -L. and Chang, R. K.: Fluorescence spectra of atmospheric aerosol at Adelphi,
1055 Maryland, USA: Measurement and classification of single particles containing organic carbon, *Atmos.*
1056 *Environ.*, 38(11), 1657–1672, doi:10.1016/j.atmosenv.2003.11.017, 2004.

1057 Pöhlker, C., Huffman, J. A. and Pöschl, U.: Autofluorescence of atmospheric bioaerosols – fluorescent biomolecules
1058 and potential interferences, *Atmos. Meas. Tech.*, 5(1), 37–71, doi:10.5194/amt-5-37-2012, 2012.

1059 Pöhlker, C., Huffman, J. A., Förster, J.-D. and Pöschl, U.: Autofluorescence of atmospheric bioaerosols: spectral
1060 fingerprints and taxonomic trends of pollen, *Atmos. Meas. Tech.*, 6(12), 3369–3392, 2013.

1061 Pöschl, U.: Atmospheric Aerosols: Composition, Transformation, Climate and Health Effects, *Angew. Chemie Int. Ed.*,
1062 44(46), 7520–7540, doi:10.1002/anie.200501122, 2005.

1063 Pöschl, U. and Shiraiwa, M.: Multiphase Chemistry at the Atmosphere–Biosphere Interface Influencing Climate and
1064 Public Health in the Anthropocene, *Chem. Rev.*, 115(10), 4440–4475, doi:10.1021/cr500487s, 2015.

1065 Reid, J. S., Jonsson, H. H., Maring, H. B., Smirnov, A., Savoie, D. L., Cliff, S. S., Reid, E. A., Livingston, J. M., Meier,
1066 M. M. and Dubovik, O.: Comparison of size and morphological measurements of coarse mode dust particles
1067 from Africa, *J. Geophys. Res. Atmos.*, 108(D19), 2003.

1068 Reponen, T., Grinshpun, S. A., Conwell, K. L., Wiest, J. and Anderson, M.: Aerodynamic versus physical size of spores:
1069 measurement and implication for respiratory deposition, *Grana*, 40(3), 119–125, 2001.

1070 Richards-Kortum, R. and Sevick-Muraca, E.: Quantitative optical spectroscopy for tissue diagnosis, *Annu. Rev. Phys.*
1071 *Chem.*, 47(1), 555–606, 1996.

1072 Rijgersberg, C. P., Van Grondelle, R. and Amesz, J.: Energy transfer and bacteriochlorophyll fluorescence in purple
1073 bacteria at low temperature, *Biochim. Biophys. Acta (BBA)-Bioenergetics*, 592(1), 53–64, 1980.

1074 Robinson, E. S., Gao, R.-S., Schwarz, J. P., Fahey, D. W. and Perring, A. E.: Fluorescence calibration method for single-
1075 particle aerosol fluorescence instruments, *Atmos. Meas. Tech.*, 10(5), 1755–1768, 2017.

1076 Robinson, N. H., Allan, J. D., Huffman, J. A., Kaye, P. H., Foot, V. E. and Gallagher, M. W.: Cluster analysis of WIBS
1077 single-particle bioaerosol data, *Atmos. Meas. Tech.*, 2013.

1078 Ruske, S., Topping, D. O., Foot, V. E., Kaye, P. H., Stanley, W., Crawford, I. P., Morse, A. and Gallagher, M. W.:
1079 Evaluation of machine learning algorithms for classification of primary biological aerosol using a new UV-LIF
1080 spectrometer, *Atmos. Meas. Tech.*, 2017.

1081 Saari, S., Reponen, T. and Keskinen, J.: Performance of Two Fluorescence-Based Real-Time Bioaerosol Detectors:
1082 BioScout vs. UVAPS, *Aerosol Sci. Technol.*, 48(4), 371–378, doi:10.1080/02786826.2013.877579, 2014.

1083 Saari, S. E., Putkiranta, M. J. and Keskinen, J.: Fluorescence spectroscopy of atmospherically relevant bacterial and
1084 fungal spores and potential interferences, *Atmos. Environ.*, 71, 202–209,
1085 doi:http://dx.doi.org/10.1016/j.atmosenv.2013.02.023, 2013.

1086 Savage, N. J. and Huffman, J. A.: Evaluation of a hierarchical agglomerative clustering method applied to WIBS
1087 laboratory data for improved discrimination of biological particles by comparing data preparation techniques,
1088 *Atmos. Meas. Tech.*, 11(8), 4929–4942, 2018.

1089 Savage, N. J., Krentz, C. E., Könemann, T., Han, T. T., Mainelis, G., Pöhlker, C. and Huffman, J. A.: Systematic
1090 characterization and fluorescence threshold strategies for the wideband integrated bioaerosol sensor (WIBS)
1091 using size-resolved biological and interfering particles, *Atmos. Meas. Tech.*, 10(11), 4279–4302,
1092 doi:10.5194/amt-10-4279-2017, 2017.

1093 Schmauss, A. and Wigand, A.: *Die Atmosphäre als Kolloid*, Vieweg+Teubner Verlag, Wiesbaden., 1929.

1094 Schmidt, M. S. and Bauer, A. J. R.: Preliminary correlations of feature strength in spark-induced breakdown
1095 spectroscopy of bioaerosols with concentrations measured in laboratory analyses, *Appl. Opt.*, 49(13), C101–
1096 C109, 2010.

1097 Schumacher, C. J., Pöhlker, C., Aalto, P., Hiltunen, V., Petäjä, T., Kulmala, M., Pöschl, U. and Huffman, J. A.: Seasonal
1098 cycles of fluorescent biological aerosol particles in boreal and semi-arid forests of Finland and Colorado,
1099 *Atmos. Chem. Phys.*, 13(23), 11987–12001, doi:10.5194/acp-13-11987-2013, 2013.

1100 Shaw, S. L., Yeh, E., Bloom, K. and Salmon, E. D.: Imaging green fluorescent protein fusion proteins in *Saccharomyces*
1101 *cerevisiae*, *Curr. Biol.*, 7(9), 701–704, 1997.

1102 Sinski, J. F. and Exner, J.: Concentration dependence in the spectra of polycyclic aromatic hydrocarbon mixtures by
1103 front-surface fluorescence analysis, *Appl. Spectrosc.*, 61(9), 970–977, 2007.

1104 Sivaprakasam, V., Lin, H.-B., Huston, A. L. and Eversole, J. D.: Spectral characterization of biological aerosol particles
1105 using two-wavelength excited laser-induced fluorescence and elastic scattering measurements, *Opt. Express*,
1106 19(7), 6191–6208, doi:10.1364/OE.19.006191, 2011.

1107 Sodeau, J. R. and O'Connor, D. J.: *Bioaerosol Monitoring of the Atmosphere for Occupational and Environmental*
1108 *Purposes*, *Compr. Anal. Chem.*, 2016.

1109 Stanley, W. R., Kaye, P. H., Foot, V. E., Barrington, S. J., Gallagher, M. and Gabey, A.: Continuous bioaerosol
1110 monitoring in a tropical environment using a UV fluorescence particle spectrometer, *Atmos. Sci. Lett.*, 12(2),
1111 195–199, doi:10.1002/asl.310, 2011.

1112 Swanson, B. E. and Huffman, J. A.: Development and characterization of an inexpensive single-particle fluorescence
1113 spectrometer for bioaerosol monitoring, *Opt. Express*, 26(3), 3646–3660, 2018.

1114 Toprak, E. and Schnaiter, M.: Fluorescent biological aerosol particles measured with the Waveband Integrated
1115 Bioaerosol Sensor WIBS-4: laboratory tests combined with a one year field study, *Atmos. Chem. Phys.*, 13(1),
1116 225–243, 2013.

1117 Twohy, C. H., McMeeking, G. R., DeMott, P. J., McCluskey, C. S., Hill, T. C. J., Burrows, S. M., Kulkarni, G. R.,
1118 Tanarhte, M., Kafle, D. N. and Toohey, D. W.: Abundance of fluorescent biological aerosol particles at
1119 temperatures conducive to the formation of mixed-phase and cirrus clouds, *Atmos. Chem. Phys.*, 16(13), 8205–

1120 8225, 2016.

1121 Von der Weiden, S. L., Drewnick, F. and Borrmann, S.: Particle Loss Calculator—a new software tool for the assessment
1122 of the performance of aerosol inlet systems, *Atmos. Meas. Tech.*, 2(2), 479–494, 2009.

1123 Welschmeyer, N. A.: Fluorometric analysis of chlorophyll a in the presence of chlorophyll b and pheopigments, *Limnol.*
1124 *Oceanogr.*, 39(8), 1985–1992, 1994.

1125 Yao, M.: *Bioaerosol: A bridge and opportunity for many scientific research fields*, 2018.

1126 Ziemba, L. D., Beyersdorf, A. J., Chen, G., Corr, C. A., Crumeyrolle, S. N., Diskin, G., Hudgins, C., Martin, R.,
1127 Mikoviny, T. and Moore, R.: Airborne observations of bioaerosol over the Southeast United States using a
1128 wideband integrated bioaerosol sensor, *J. Geophys. Res. Atmos.*, 121(14), 8506–8524, 2016.

1129

1130 **Appendix A:** List of acronyms and symbols.

Acronym/Symbol	Description
AF	Asymmetry factor
APC	Airborne Particle Classifier
CCD	Charge-coupled device
DMT	Droplet Measurement Technologies
EEM	Excitation-emission matrix
EM	Emission
EX	Excitation
IR	Infrared
LIF	Light-induced fluorescence
<i>N</i>	Particle number concentration (cm^{-3})
<i>N_{T,c}</i>	<i>N</i> of total coarse particles (1-20 μm)
<i>N_{F,c(nσ)}</i>	<i>N</i> of fluorescent coarse particles (1-20 μm) at 1, 3, or 6 σ
NAD	Nicotinamide adenine dinucleotide
NAD(P)H	Nicotinamide adenine dinucleotide and nicotinamide adenine dinucleotide phosphate
NIST	National institute of standards and technology
PBAP	Primary biological aerosol particles
PMT	Photomultiplier tube
PAH	Polycyclic aromatic hydrocarbons
PSL	Polystyrene latex sphere
PS-DVB	Polystyrene-divinylbenzene
SD	Standard deviation
SIBS	Spectral intensity bioaerosol sensor
SNR	Signal to noise ratio
TSP	Total suspended particles
UV	Ultraviolet
UV-APS	Ultraviolet aerodynamic particle sizer
Vis	Visible light
WIBS	Wideband integrated bioaerosol sensor

1131

1132 **Table 1.** Lower, mean, and upper wavelength at each PMT detection channel. Nominal data accord-
 1133 ing to manufacturer Hamamatsu.

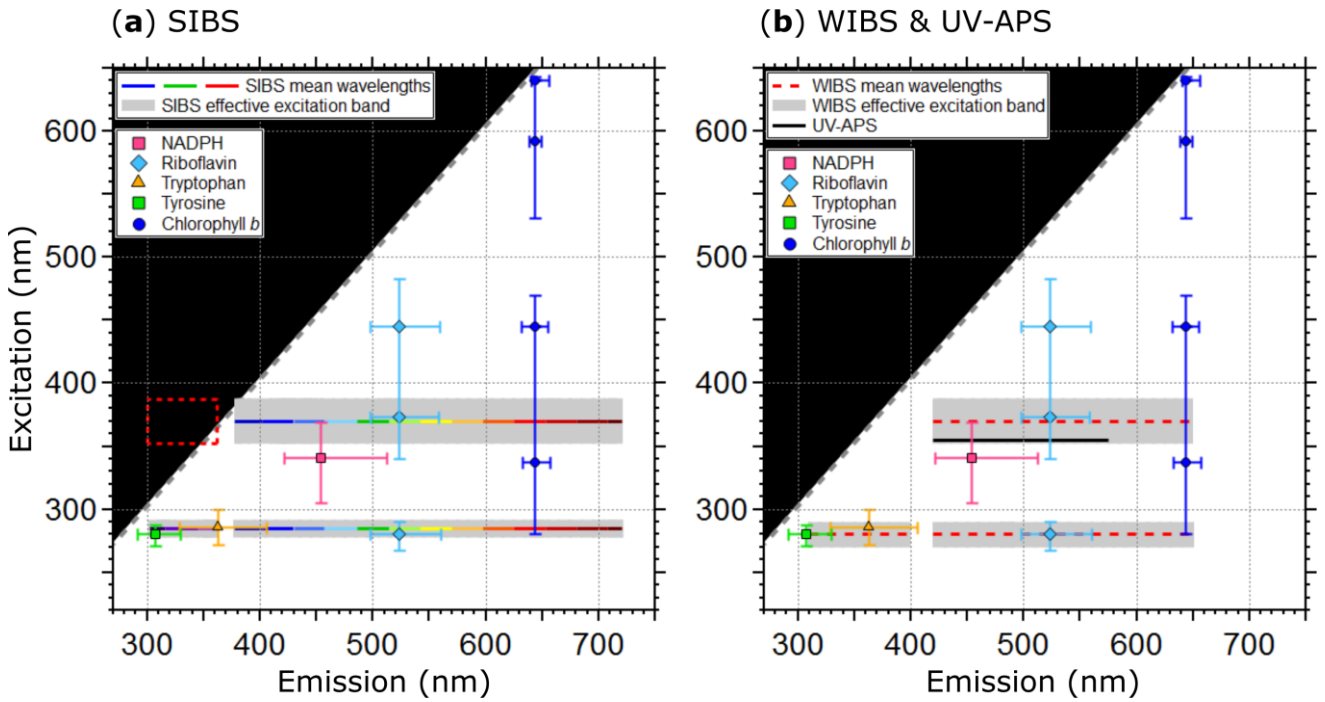
Channel	λ_{lower} (nm)	λ_{mean} (nm)	λ_{upper} (nm)
1	298.2	302.2	316.2
2	316.6	330.6	344.6
3	345.0	359.0	362.5
4	377.5	387.3	401.3
5	401.5	415.6	429.7
6	429.8	443.8	457.8
7	457.9	471.9	485.9
8	486.0	500.0	514.0
9	514.0	528.0	542.0
10	541.9	555.9	569.9
11	569.7	583.7	597.7
12	597.4	611.4	625.4
13	625.0	639.0	653.0
14	652.8	666.5	680.2
15	679.9	693.9	707.9
16	707.1	721.1	735.1

1134 **Table 2.** Parameters and technical components of the SIBS in comparison to the WIBS-NEO and
 1135 WIBS-4A. Data are taken from manufacturer information.

	SIBS	WIBS-NEO	WIBS-4A
First production	2015	2016	2009
Measured parameters	Particle size Asymmetry Factor Fluorescence spectra	Particle size Asymmetry Factor Integrated fluorescence in 3 channels	Particle size Asymmetry Factor Integrated fluorescence in 3 channels
Particle size range	~0.3 – 100 μm	~0.5 – 30 μm	~0.5 – 20 μm
Maximum concentration	$\sim 2 \times 10^4$ particles/L	$\sim 2 \times 10^4$ particles/L	$\sim 2 \times 10^4$ particles/L
Fluorescence excitation	$\lambda_{\text{ex}} = 285$ and $\lambda_{\text{ex}} = 370$ nm	$\lambda_{\text{ex}} = 280$ and $\lambda_{\text{ex}} = 370$ nm	$\lambda_{\text{ex}} = 280$ and $\lambda_{\text{ex}} = 370$ nm
Fluorescence emission	$\lambda_{\text{mean}} = 302 - 721$ nm (16-channel PMT)	$\lambda_{\text{em}} = 310-400$ nm and $\lambda_{\text{em}} = 420-650$ nm	$\lambda_{\text{em}} = 310-400$ nm and $\lambda_{\text{em}} = 420-650$ nm
Flow rate	Sample flow: ~0.3 l/min Sheath flow: ~2.2 l/min (re-circulating)	Sample flow: ~0.3 l/min Sheath flow: ~2.2 l/min (re-circulating)	Sample flow: ~0.3 l/min Sheath flow: ~2.2 l/min (re-circulating)
Laser	785 nm diode laser, 55 mW	635 nm diode laser, 15 mW	635 nm diode laser, 12 mW
Pump	Diaphragm pump	Diaphragm pump	Diaphragm pump
Power requirements	200 W, 90 - 230 VAC	150 W, 90 - 230 VAC	150 W, 90 - 230 VAC
Weight (kg)	20.1	12.5	13.6
Dimension W x L x H (cm)	42.5 x 61.5 x 23.5	45.1 x 36.2 x 24.1	30.4 x 38.2 x 17.1

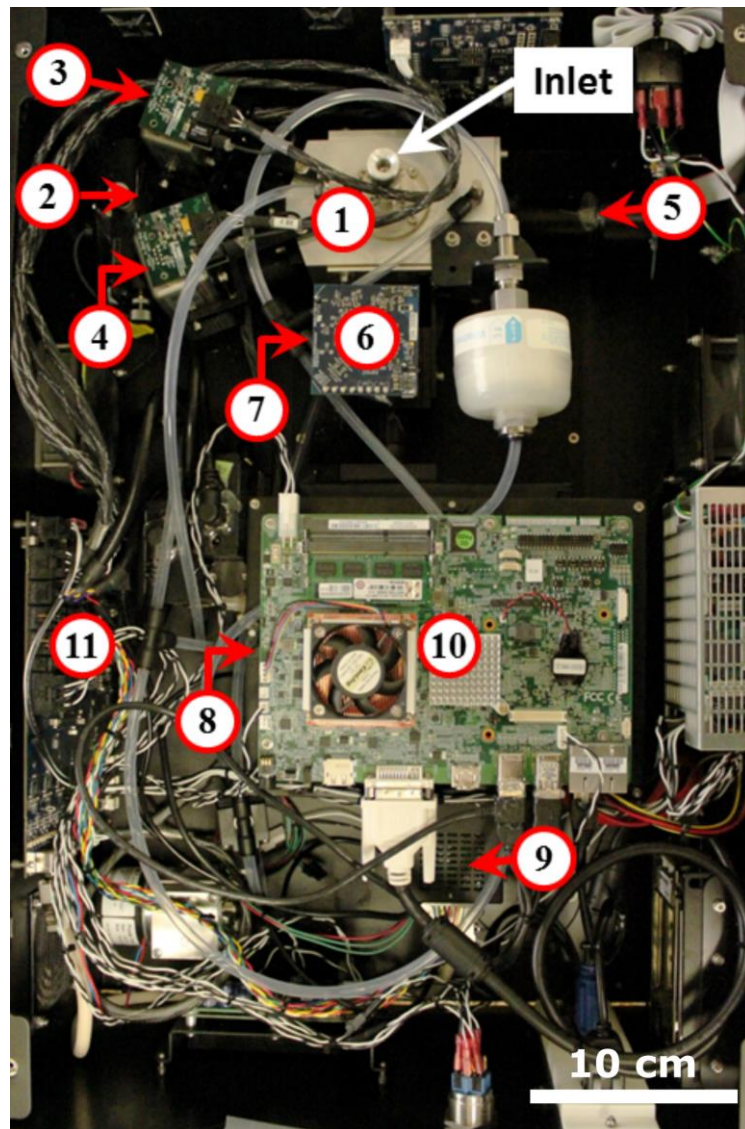
1136 **Table 3.** Asymmetry factor (AF) values for reference particles. Values are based on the mean of a
1137 Gaussian fit applied onto each particle histogram (see also Fig. 10), including 1σ SD.

	AF
2 μm non-fluorescent PSLs	9.9 ± 3.6
Ultrapure water	11.9 ± 2.9
Ammonium sulfate	13.1 ± 8.1
Fe₃O₄	14.4 ± 7.4
Carbon nanotubes	21.6 ± 12.7

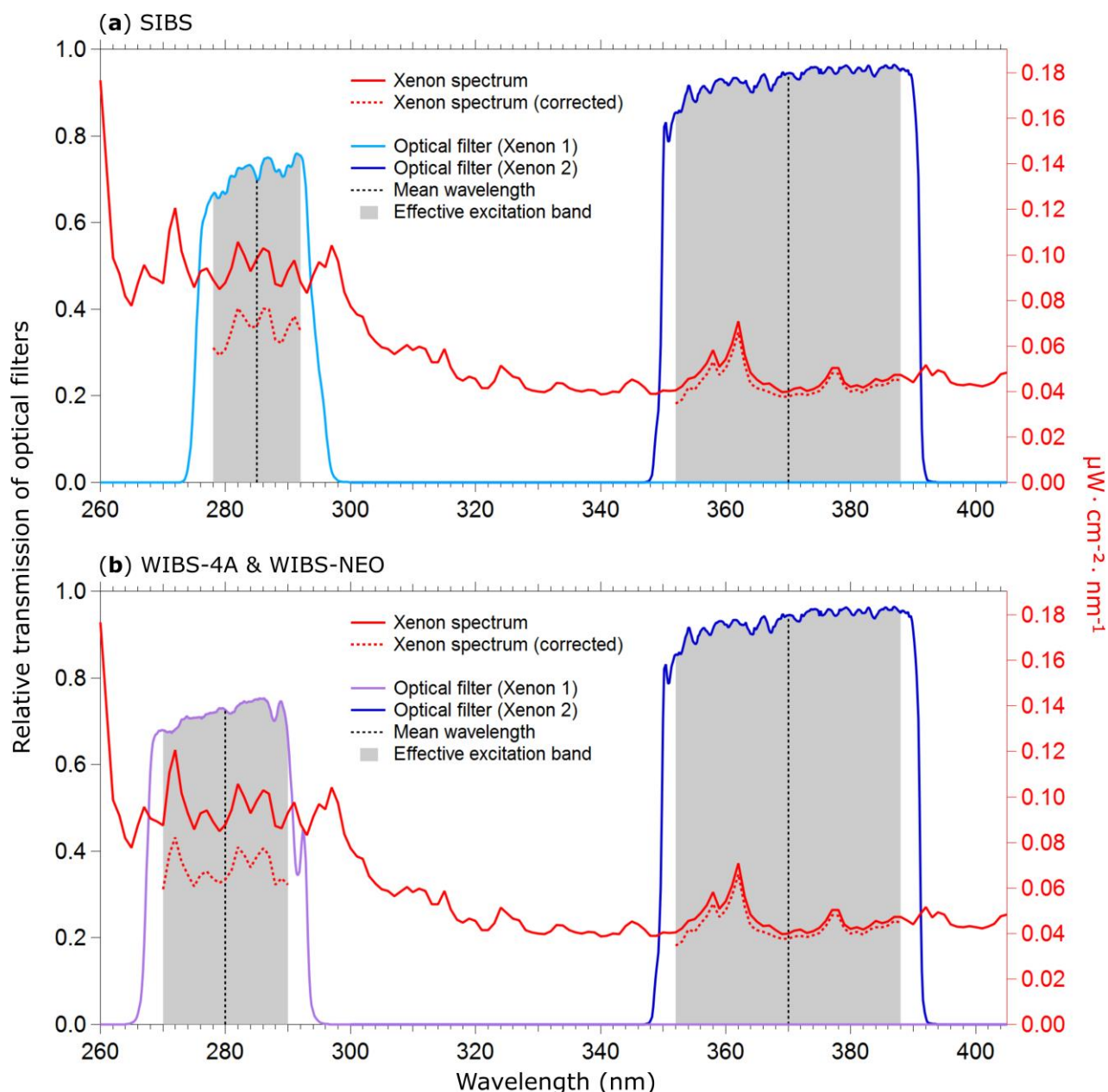


1138 **Figure 1.** Optical design and overview of excitation and emission specifications of the LIF instru-
 1139 ments UV-APS, WIBS, and the SIBS with spectral locations of the autofluorescence modes of the
 1140 biofluorophores tyrosine, tryptophan, NAD(P)H, riboflavin, and chlorophyll *b* (as examples). Here
 1141 the term WIBS includes the WIBS-4A and WIBS-NEO, because both instruments use the same opti-
 1142 cal components. Spectral properties of the emission bands of LIF instruments are illustrated as hori-
 1143 zontal lines. The color-coded bars in (a) illustrate the spectrally resolved fluorescence detection of
 1144 the two excitation wavelengths ($\lambda_{ex} = 285$ and 370 nm) by the SIBS. The “blind spot” (white notch)
 1145 at $\lambda_{ex} = 285$ nm between $\lambda_{em} = 362 - 377$ nm (a) originates from a notch optical filter, used to block
 1146 incident light from the excitation sources. Grey dashed lines show the 1st order elastic scattering. At
 1147 $\lambda_{ex} = 370$ nm, the detection range of the SIBS includes the spectral range where $\lambda_{em} < \lambda_{ex}$, for which
 1148 fluorescence is not defined and so data within the red dashed rectangle is omitted (a). Grey bars
 1149 indicate the effective excitation bands of optical filters used for the WIBS and SIBS (see also Sect.
 1150 3.3 and Fig. 3). The effective excitation bands in the WIBS and SIBS occur in a spectral range span-
 1151 ning several nanometers (up to 36 nm), in contrast to the UV-APS (black line, b), which uses a laser
 1152 source with a defined excitation (Figure adapted from Pöhlker et al., 2012).

1153
1154
1155
1156
1157
1158
1159
1160
1161
1162
1163
1164
1165
1166

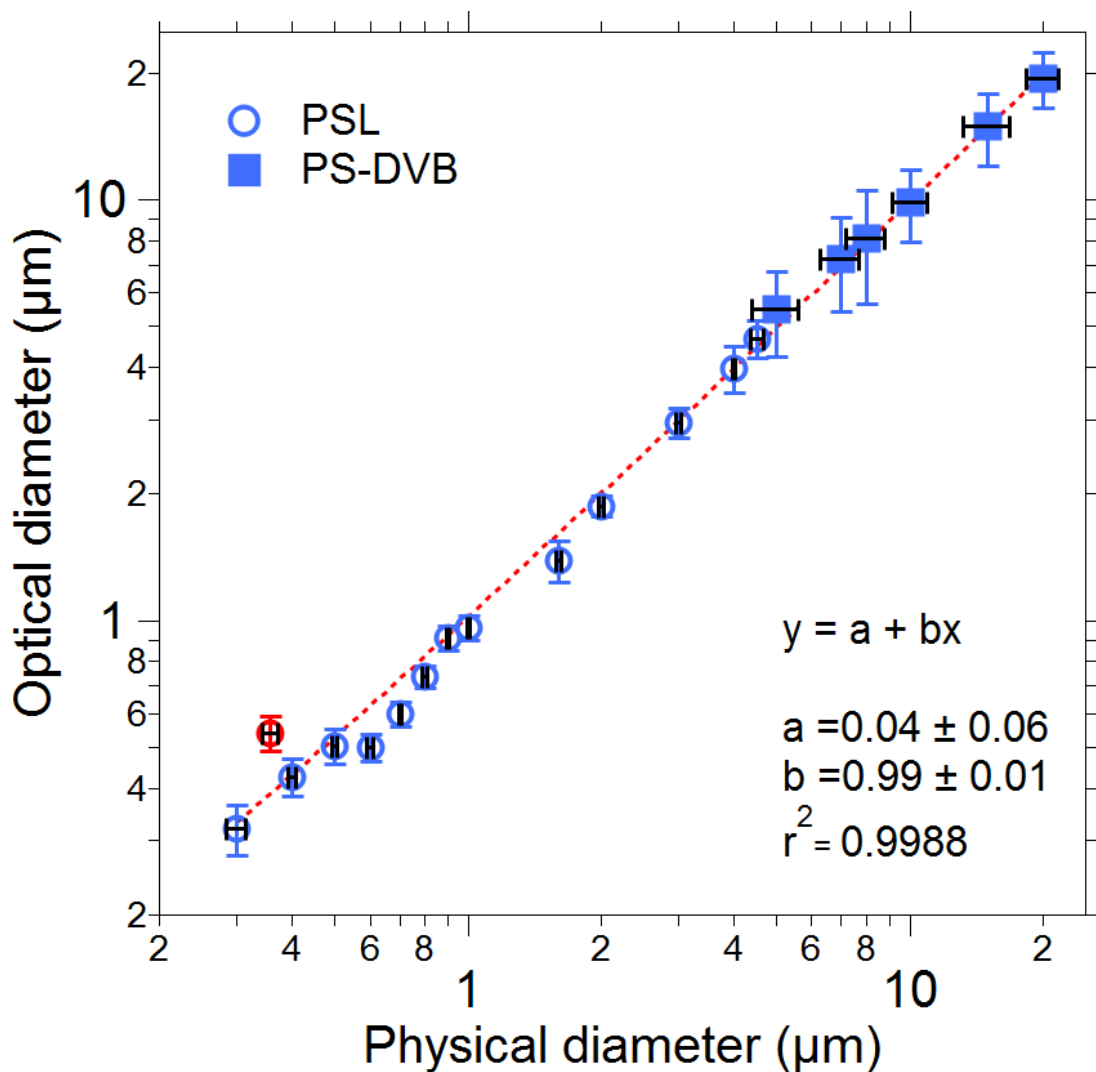


1167 **Figure 2.** Technical components within SIBS body. (1) Optical cavity. (2) Continuous wave diode
1168 laser used for particle detection and sizing. (3) and (4) Xenon light sources. (5) Quadrant PMT used
1169 for the determination of particle asymmetry. (6) PMT used for particle detection and sizing. (7) Di-
1170 chroic beamsplitter separates side-scattered light (particle sizing) and fluorescence emission (not vis-
1171 ible; below component (6)). (8) Grating polychromator (below component (10)). (9) 16-channel PMT
1172 used for detection of fluorescence. (10) Embedded computer unit. (11) Control-board.

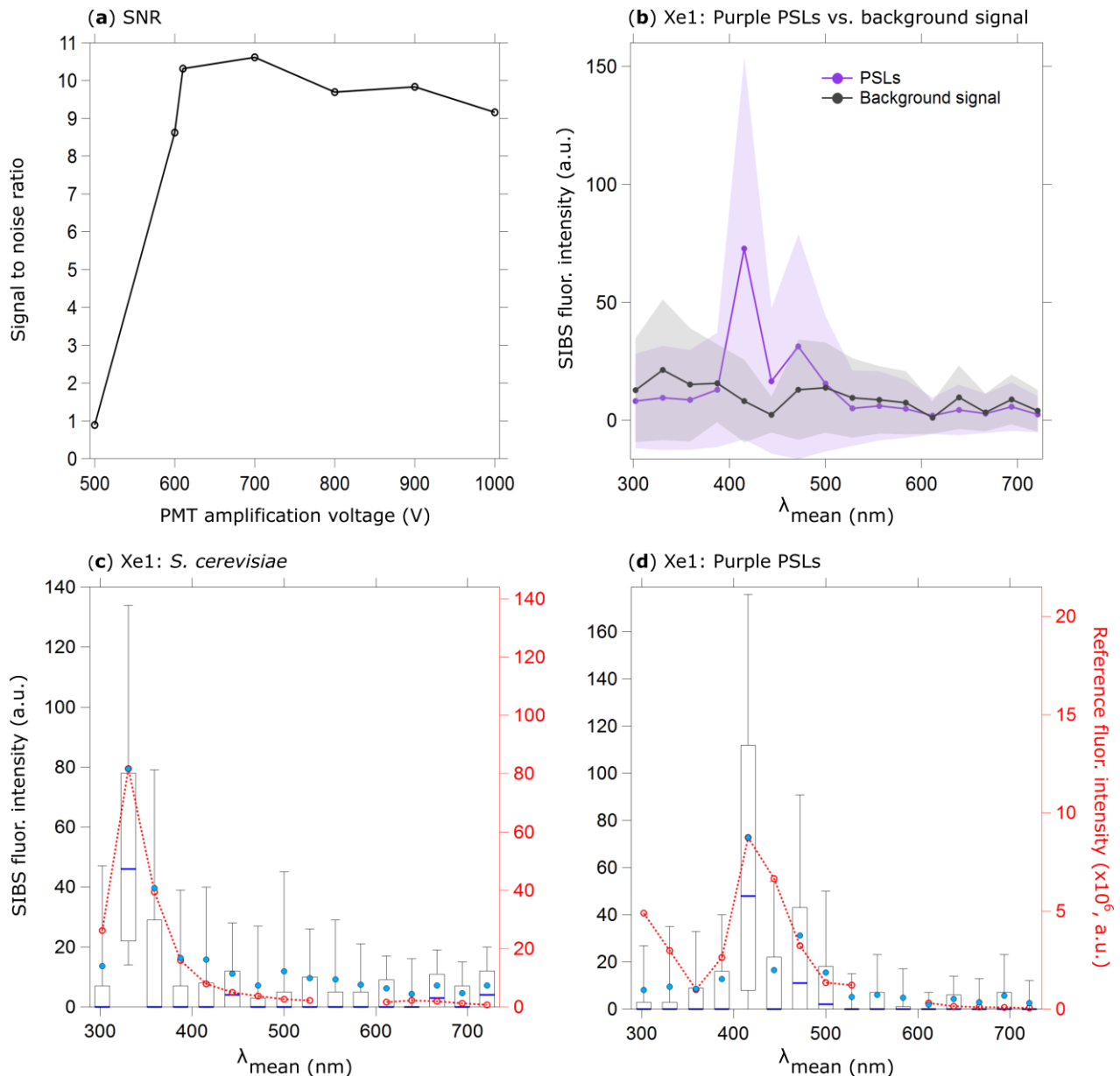


1173 **Figure 3.** Irradiance from xenon flash lamps based on specifications of lamps and optical filters.
 1174 Purple and blue lines show optical transmission of filters (left axes) applied to select excitation wave-
 1175 length. Gray bands indicate where filter transmit light relative from the mean wavelength. Red lines
 1176 show theoretical irradiance values of the xenon flash lamp (right axes): solid line (raw output), dashed
 1177 line (relative output after filtering). Relative output shown as raw output multiplied by effective ex-
 1178 citation band of the bandpass filters used in the: (a) SIBS ($\Delta\lambda_{\text{ex}}(\text{Xenon1}) = \sim 14$ nm; $\Delta\lambda_{\text{ex}}(\text{Xenon2}) = \sim 36$
 1179 nm), and (b) WIBS-4A and WIBS-NEO ($\Delta\lambda_{\text{ex}}(\text{Xenon1}) = \sim 20$ nm; $\Delta\lambda_{\text{ex}}(\text{Xenon2}) = \sim 36$ nm). Xenon lamp
 1180 operating conditions: 600 V main voltage, 0.22 μF main capacitance, 126 Hz repetition rate, 500 mm
 1181 distance. (Data courtesy: Xenon flash lamps / Hamamatsu; Single-band bandpass filters / Semrock).

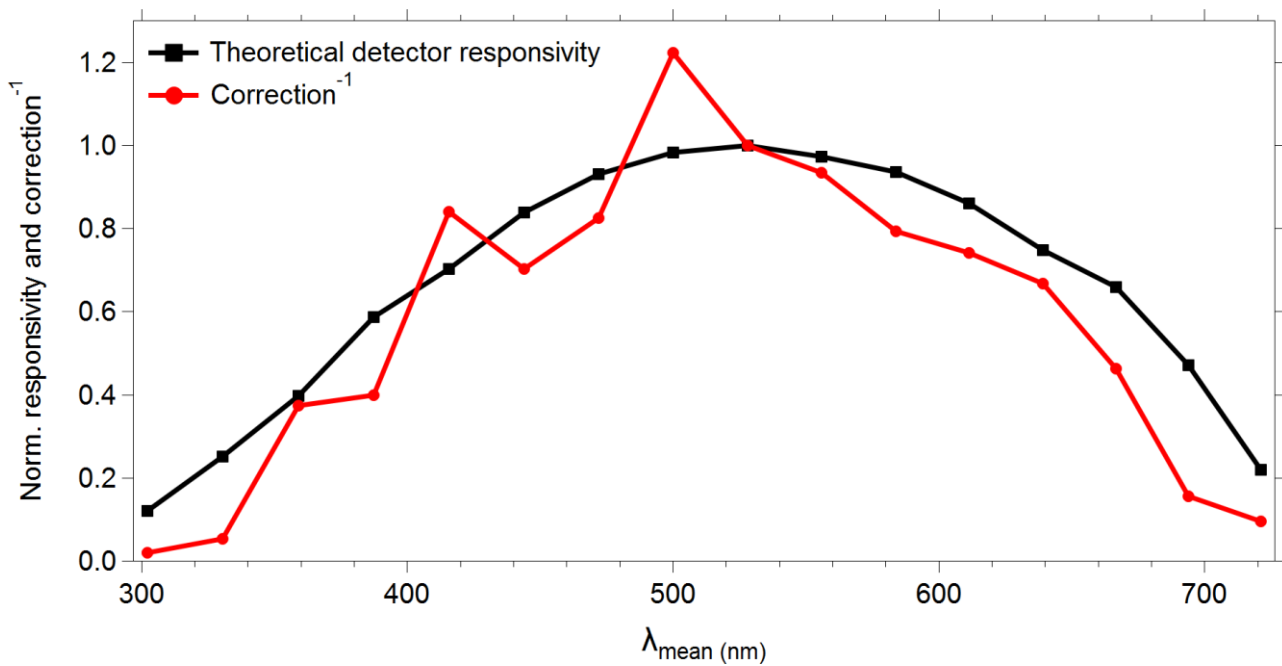
1182
1183
1184
1185
1186
1187
1188
1189
1190
1191
1192
1193
1194



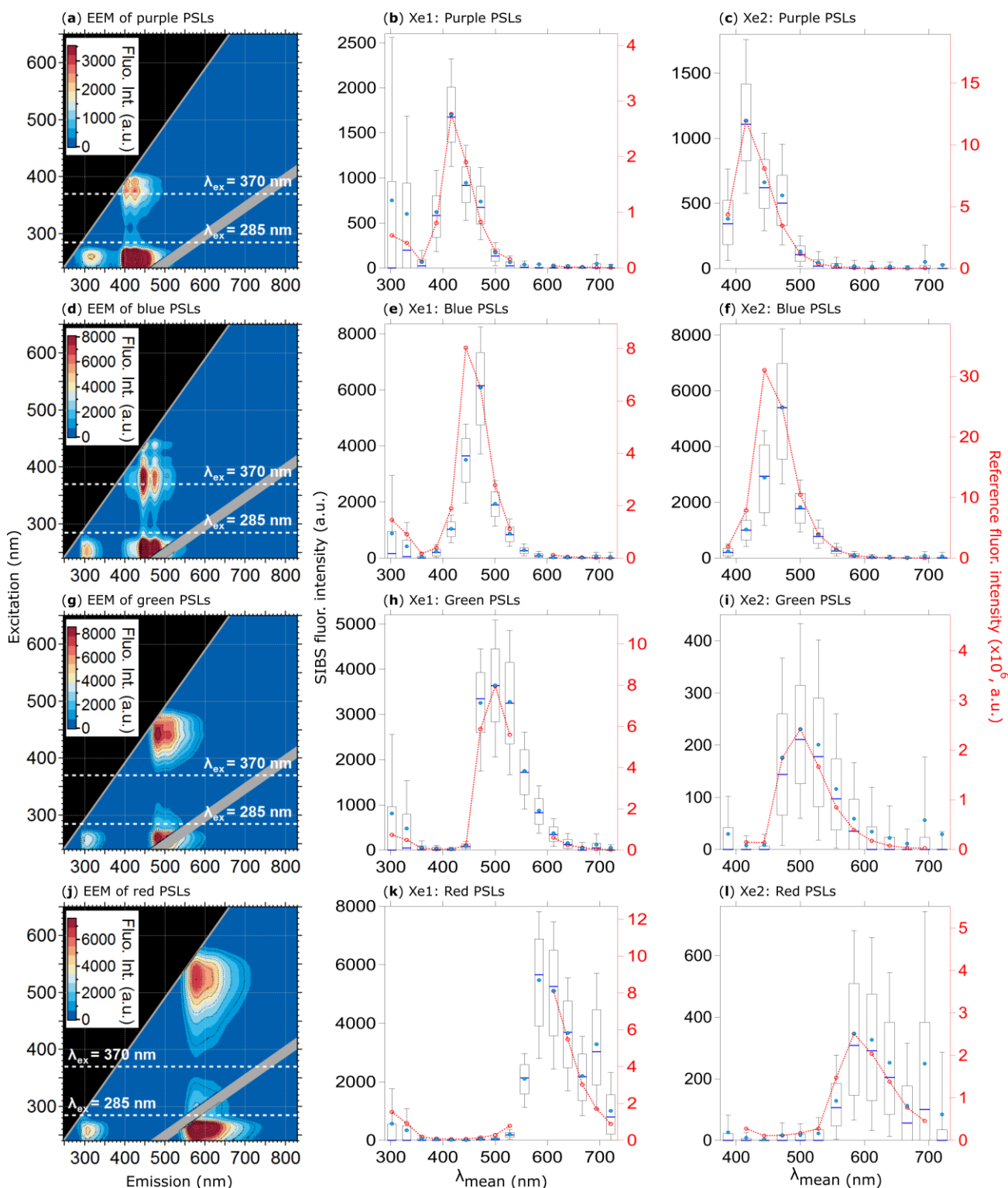
1195 **Figure 4.** Size calibration of SIBS. Black horizontal bars indicate 1σ SD as stated by each manufac-
1196 turer (Table S1). Optical diameter values and related 1σ SD are based on a Gaussian fit, which was
1197 used to average size distributions of several thousand homogeneous particles for each measurement.
1198 The linear fit (red dashed line) excludes the $0.356\ \mu\text{m}$ PSL sample (red marker), an outlier potentially
1199 caused by a poor quality PSL batch. Only non-fluorescent particle standards were used for determin-
1200 ing the sizing accuracy.



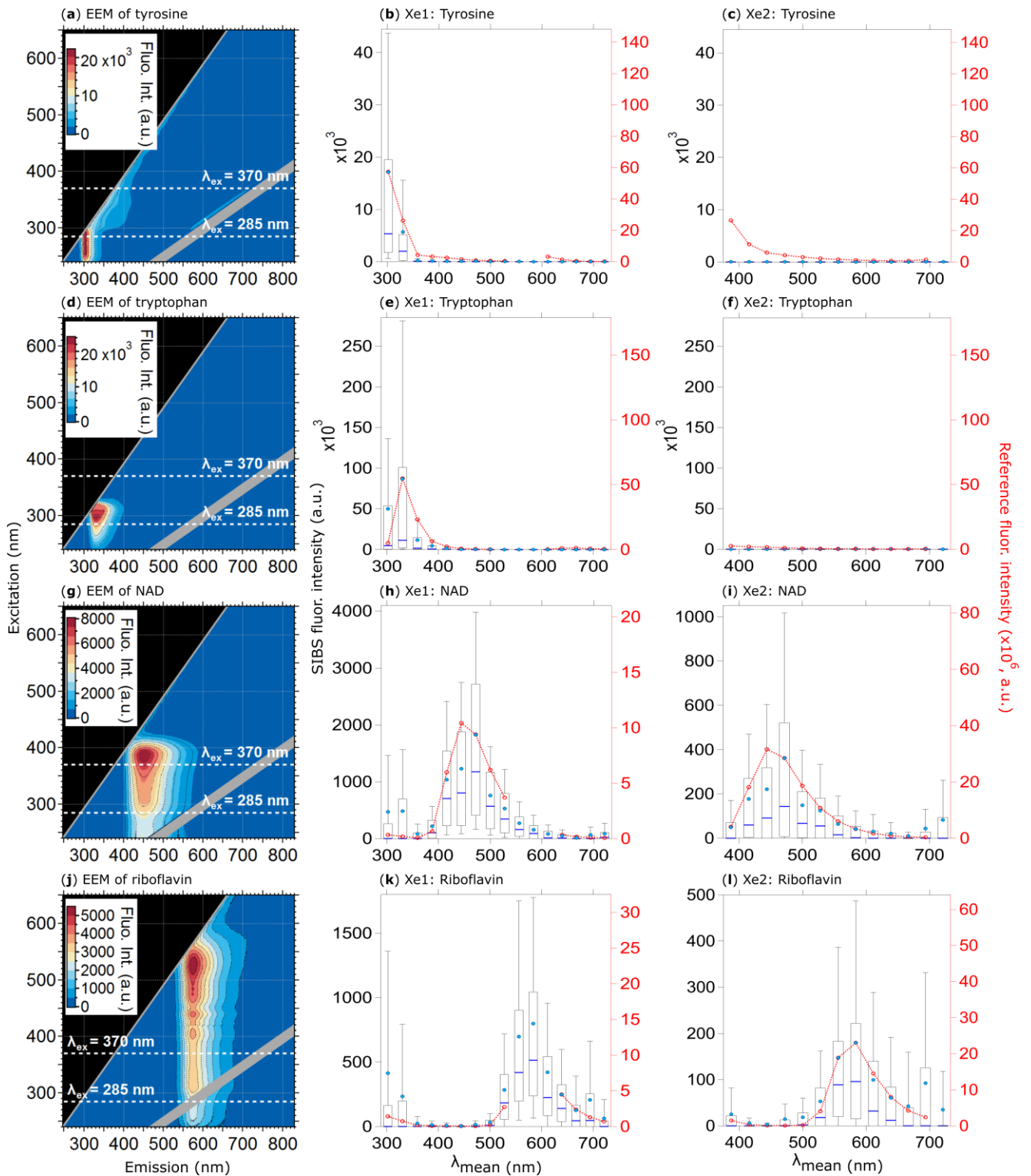
1201 **Figure 5.** SIBS signal to noise ratio (SNR) in (a): emission of $0.53 \mu\text{m}$ purple PSLs (5260 particles,
 1202 background signal + 1σ SD subtraction) divided by background signal at different PMT amplification
 1203 voltages (both at Xe1, channel 5, averaged, and uncorrected). Background signal measured over 5
 1204 min. In (b), fluorescence emission in contrast to background signal at a PMT amplification voltage
 1205 of 610 V are shown (same parameters as in (a)). Shaded area: 1σ SD. Fluorescence intensity values
 1206 are shown in arbitrary units. Fluorescence emission spectra of (c) *S. cerevisiae* (yeast; 2048 particles,
 1207 $0.5 - 1 \mu\text{m}$) and (d) PSLs (as in (b)). Red dashed lines and markers (right axes) show averaged and
 1208 re-binned reference spectra. Box and whisker plots (left axes) show SIBS spectra: median (blue line),
 1209 mean (circle), boxes 75 and 25 percentile, whiskers 90 and 10 percentile. Data coinciding with 1st or
 1210 2nd order elastic scattering were removed from reference spectra.



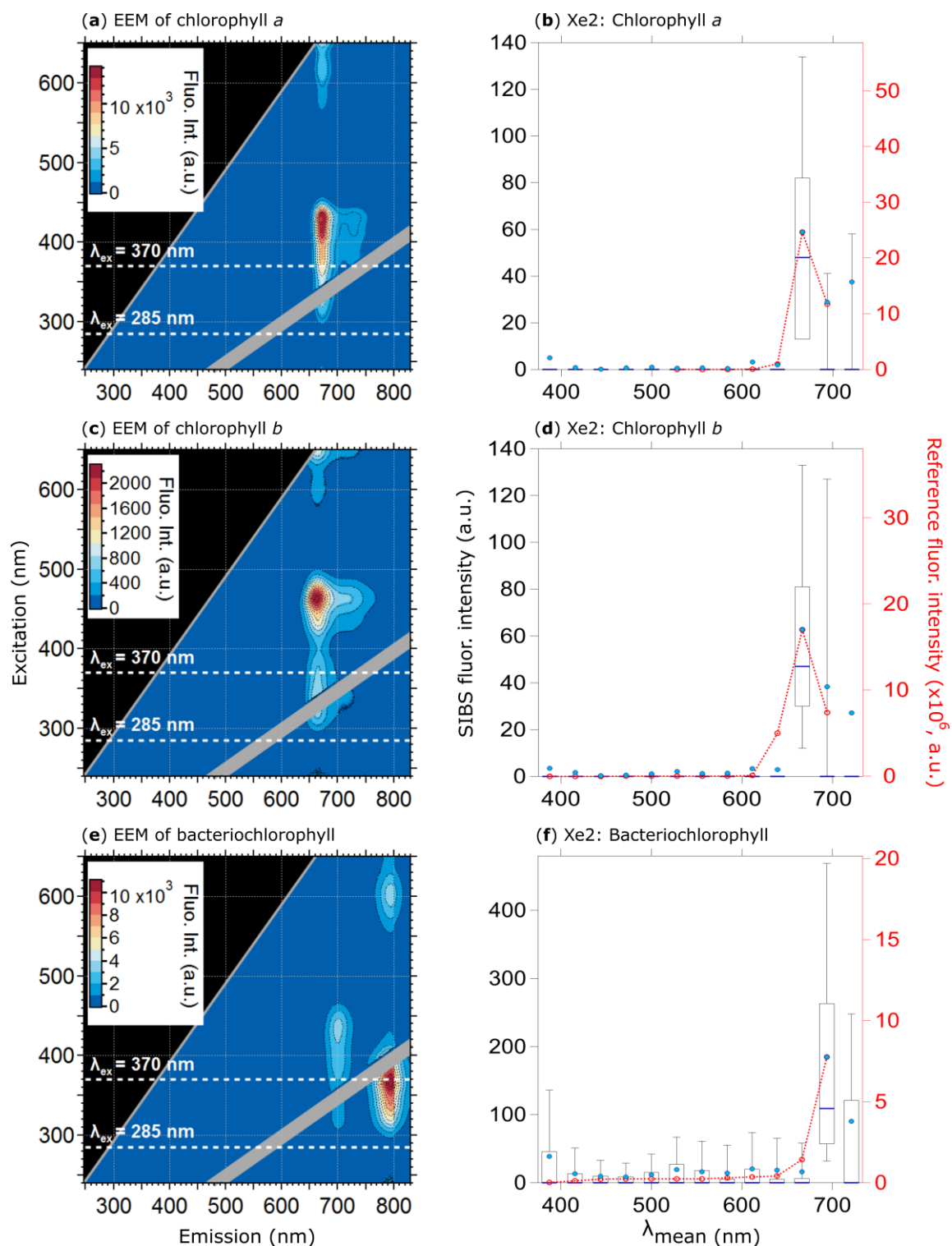
1211 **Figure 6.** Normalized theoretical detector responsivity and spectral correction. Theoretical detector
 1212 responsivity derived from measured cathode radiant sensitivity multiplied by the diffraction effi-
 1213 ciency (as shown in Figure S8). Note that red line shows inverse of spectral correction to match
 1214 detector response.



1215 **Figure 7.** Fluorescence emission spectra of PSLs. Steady-state fluorescence signatures displayed as
 1216 EEMs (left column) and spectra at Xe1 and Xe2 (middle, right columns) for: 2.07 μm purple (**a**, **b**
 1217 and **c**, 1082 particles), 2.1 μm blue (**d**, **e** and **f**, 1557 particles), 2 μm green (**g**, **h**, and **i**, 1174 particles),
 1218 and 2 μm red PSLs (**j**, **k**, and **l**, 1474 particles). Within EEMs: white dashed lines show SIBS excita-
 1219 tion wavelengths ($\lambda_{\text{ex}} = 285$ and 370 nm), grey diagonal lines indicate 1st and 2nd order elastic scat-
 1220 tering bands (both bands were subtracted automatically by the Aqualog V3.6 software). Red dashed
 1221 lines and markers (right axes; middle, right columns): averaged and re-binned reference spectra.

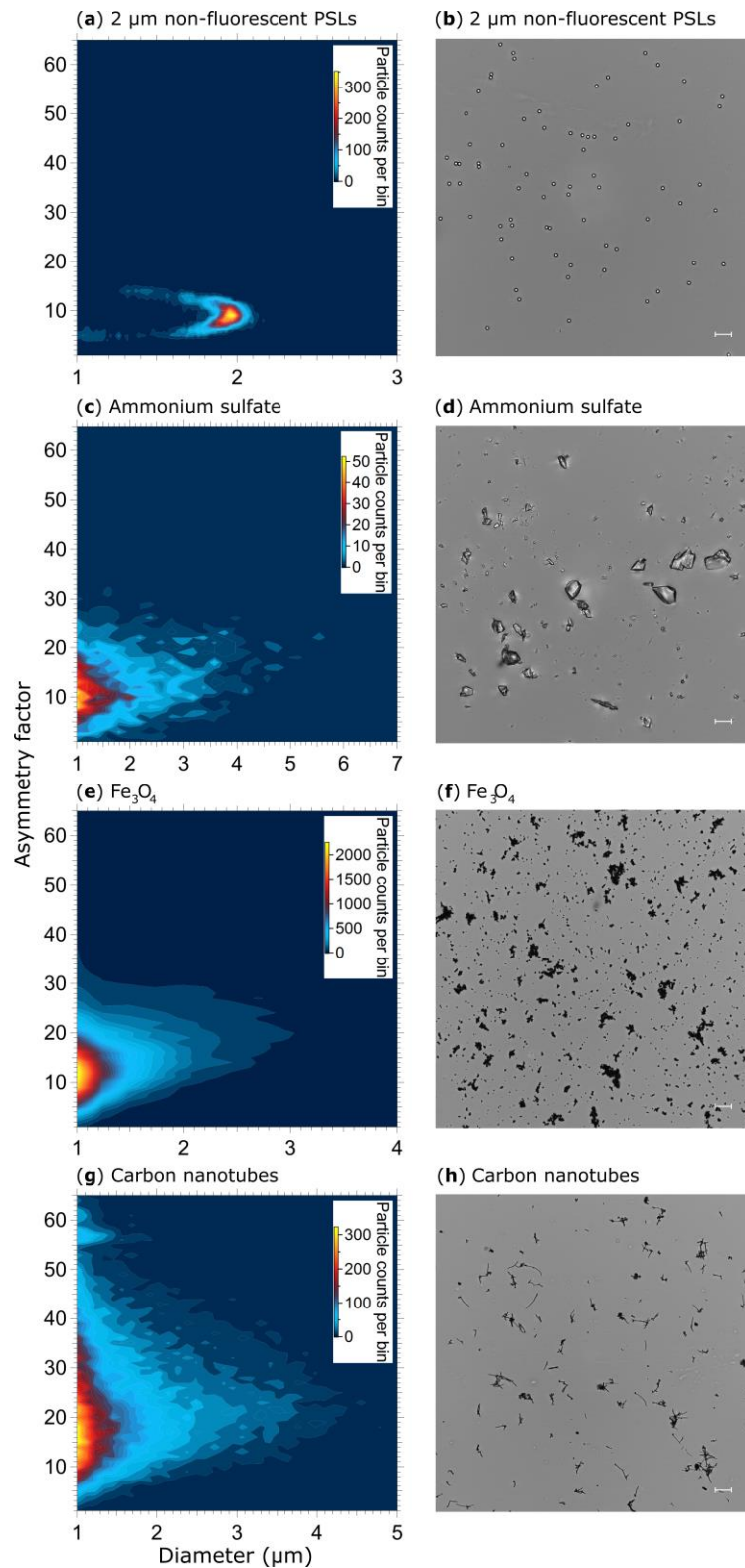


1222 **Figure 8.** Fluorescence emission spectra of biofluorophores. EEMs (left column) and spectra at Xe1
 1223 and Xe2 wavelengths (middle and right columns) shown for: tyrosine (a, b, and c, 209 particles),
 1224 tryptophan (d, e, and f, 193 particles), NAD (g, h, and i, 376 particles), and riboflavin (j, k, and l,
 1225 205 particles). Red dashed lines and markers (right axes; middle, right columns): averaged and re-
 1226 binned reference spectra. All biofluorophores were size-selected between 1 and 2 μm .

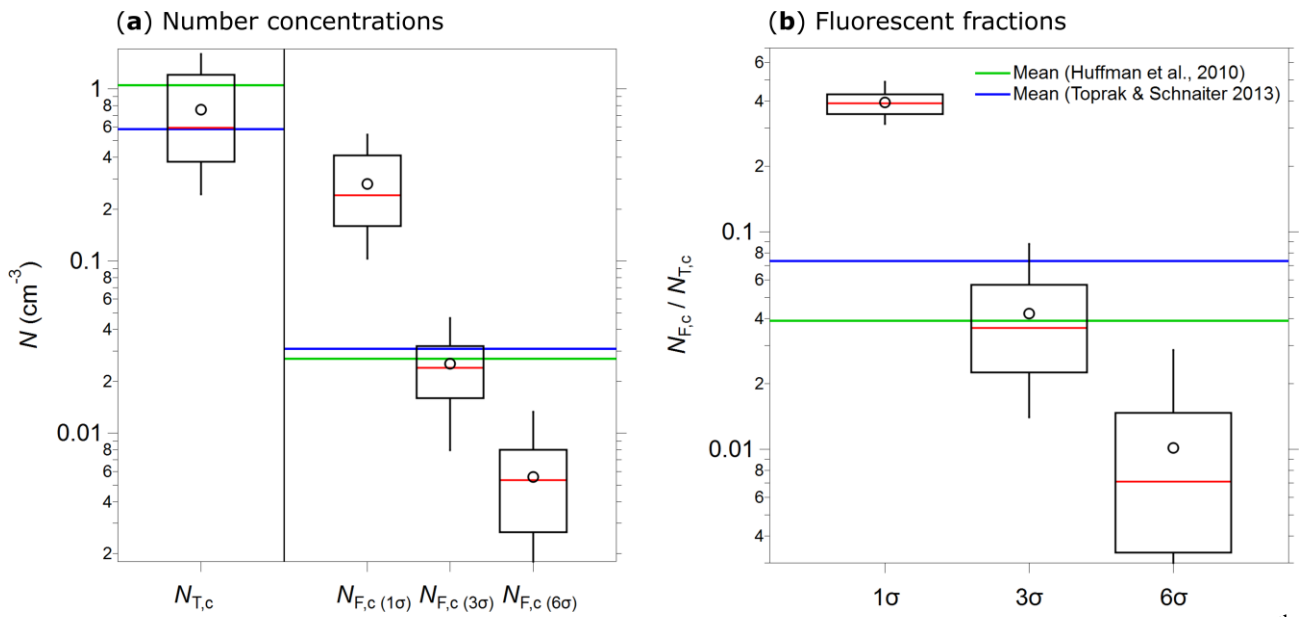


1227 **Figure 9.** Fluorescence emission spectra of three chlorophyll types. Highlighted are EEMs (left col-
 1228 umn) and spectra at Xe2 (right columns) for: chlorophyll *a* (a and b, 370 particles), chlorophyll *b* (c
 1229 and d, 585 particles), and bacteriochlorophyll (e and f, 633 particles). Red dashed lines and markers
 1230 (right axes; right column): averaged and re-binned reference spectra. Size range chlorophyll *a* and *b*:
 1231 0.5 - 2 μm , size range bacteriochlorophyll: 0.5 - 1 μm . Emission spectra at Xe1 are excluded due to
 1232 a fluorescence artifact caused by solved components from the polymer of the aerosolization bottles
 1233 (Fig. S12).

1234
1235
1236
1237
1238
1239
1240
1241
1242
1243
1244
1245
1246
1247
1248
1249
1250
1251
1252
1253
1254
1255
1256
1257
1258
1259
1260
1261
1262



1263 **Figure 10.** Particle asymmetry. Shown are particle density histograms (left column) and microscopy
1264 images (right column) for: 2 μm non-fluorescent PSLs (**a** and **b**, 17836 particles), ammonium sulfate
1265 (**c** and **d**, 3496 particles), Fe_3O_4 (**e** and **f**, 65097 particles), and carbon nanotubes (56949 particles, **g**).
1266 Scale bar (right column) indicates a length of 10 μm .



1267 **Figure 11.** Integrated coarse particle (1-20 μm) number concentrations, measured between the 12th
 1268 and 18th of April 2018 (5 min average), for total particles ($N_{T,c}$, fluorescent and non-fluorescent) and
 1269 coarse fluorescent particles ($N_{F,c}$) after 1, 3, and 6 σ SD background signal subtraction (a). The fluo-
 1270 rescent fractions of integrated coarse particle number concentrations ($N_{F,c} / N_{T,c}$) at 1, 3, and 6 σ SD
 1271 are shown in (b). Median (red line), mean (black circles), boxes 75 and 25 percentile, whiskers 95
 1272 and 5 percentile (a and b). Data from Huffman et al. (2010) (green lines) and Toprak & Schnaiter,
 1273 (2013) (blue lines) were taken for comparison (a and b).